

Collision Avoidance Maneuvers Optimization in the Presence of Multiple Encounters

Zeno Pavanello*, Laura Pirovano[†] and Roberto Armellin[‡]
Te Pūnaha Ātea - The Space Institute, The University of Auckland, Auckland 1010, New Zealand

Andrea De Vittori[§] and Pierluigi di Lizia[¶]
Polytechnic University of Milan, Milan 20156, Italy

The optimization of fuel-optimal low-thrust collision avoidance maneuvers (CAMs) in scenarios involving multiple encounters between spacecraft is addressed. The optimization's objective is the minimization of the total fuel consumption while respecting constraints on the total probability of collision. The solution methodology combines sequential convex programming, second-order cone programming, and differential algebra to approximate the non-convex optimal control problem progressively. A Gaussian mixture model method is used to propagate the initial covariance matrix of the secondary spacecraft, allowing us to split it into multiple mixands that can be treated as different objects. This leads to an accurate propagation of the uncertainties. No theoretical guarantee is given for the convergence of the method to the global optimum of the original optimal control problem. Nonetheless, good performance is demonstrated through case studies involving multiple short- and long-term encounters, showcasing the generation of fuel-efficient CAMs while respecting operational constraints.

I. Introduction

Spacecraft operations are encountering growing challenges due to the proliferation of space debris and the saturation of valuable orbital regimes, notably the geostationary Earth orbit (GEO) and the low Earth orbit (LEO) ones, where large constellations reside [1]. Ensuring the safety of spacecraft has become a paramount concern. In this regard, the collision avoidance maneuver (CAM) has emerged as a critical requirement for spacecraft operators, aiming to autonomously and efficiently navigate through potentially hazardous encounters. While the existing body of research extensively addresses

*PhD candidate, Te Pūnaha Ātea - Space Institute, 20 Symonds Street, Auckland Central, Auckland 1010, New Zealand; zpav176@aucklanduni.ac.nz (Corresponding Author).

[†]Research Fellow, Te Pūnaha Ātea - Space Institute, 20 Symonds Street, Auckland Central, Auckland 1010, New Zealand; laura.pirovano@auckland.ac.nz.

[‡]Professor, Te Pūnaha Ātea - Space Institute, 20 Symonds Street, Auckland Central, Auckland 1010, New Zealand; roberto.armellin@auckland.ac.nz. Member AIAA.

[§]Ph.D. candidate, Department of Aerospace Science and Technology, Via La Masa 34, Milan 20156. Italy.

[¶]Associate Professor, Department of Aerospace Science and Technology, Via La Masa 34, Milan 20156. Italy.

A part of this work was presented at the 2024 AIAA Science and Technology Forum and Exposition, held in Orlando, Florida, January 8-12 2024. Paper AIAA-2024-0845 was entitled "A Convex Optimization Method for Multiple Encounters Collision Avoidance Maneuvers".

single short-term encounters [2–5], recent attention has shifted toward scenarios involving multiple close encounters [6–10]. This paper presents an innovative approach to address the complex problem of fuel-efficient CAMs in the context of multiple short- and long-term encounters. In short-term encounters, the problem can be simplified, and each conjunction can be framed in its B-plane, whereas this is not possible in the long-term case because the path of relative motion inside the combined covariance ellipsoid is far from rectilinear, and the encounter is not instantaneous [11].

Conventional strategies for CAM optimization primarily focus on mitigating a single short-term encounter through the reduction of the probability of collision (PoC) or the increase of the miss distance [2, 4, 5, 12–15]. Very few strategies have been developed for long-term encounters [16–18]. However, the increasing density of space debris and the prospect of multiple close encounters demand a more comprehensive and sophisticated approach. Lately, NASA is taking steps in this direction, with the introduction of the concept of total probability of collision (TPoC) [8] to quantify the contribution of multiple conjunctions to the overall collision probability: they recognize that in an environment that is densely populated, treating each conjunction as a separate event will become unsustainable for operators. The challenge lies in developing methodologies that can efficiently compute optimal trajectories while considering both onboard propulsion’s practical constraints and the encounters’ combined probabilistic nature. Regarding long-term encounters, few publications have addressed the problem of computing a CAM [16–19]. In this circumstance, instead of minimizing PoC, the alternative instantaneous probability of collision (IPoC) is controlled and kept below a certain threshold for the whole window of interest.

The multiple short-term problem has been faced in previous literature. Kim *et al.* [6] developed a genetic algorithm approach that deals with up to four conjunctions but must perform a separate Δv impulse for each encounter. Their method does not include a check on TPoC; instead, they minimize PoC of each conjunction separately. This results in a higher final TPoC, and thus the method underestimates the risk of a collision. The authors do not provide a run-time for their method, but genetic algorithms are notoriously slower to converge with respect to other methods. Sánchez and Vasile [9] developed a comprehensive tool that is based on a linear approximation of the dynamics with impulsive maneuvers and finds the optimal CAM using a min-max optimization. Their method combines machine learning and multi-criteria decision-making techniques to assess the collision risk and rank possible optimal CAMs. They propose two main strategies: either computing a single maneuver or treating each conjunction as a separate event. In the first case, only the worst-case scenario is considered; therefore, the computed impulse may not be optimal. In the second case, a separate maneuver is computed for each one of the encounters: this means that after the maneuver for the first conjunction has been computed, PoC must be re-calculated for each of the following conjunctions. This process must be repeated as many times as the number of the conjunctions. Sánchez and Vasile’s approach can be very beneficial for operators on the ground to assist in the selection of the preferable CAM for a specific scenario. Still, it cannot be used to compute autonomous maneuvers due to the high computational load and the necessary human interaction that it requires. Massòn *et al.* [10] cast the problem as a linear program (LP) with non-convex quadratic constraints, and they solve it by

preallocating the maneuvering opportunities. They linearize the dynamics using the Yamanaka-Ankersen state transition matrix (STM), and they impose linear station keeping (SK) constraints. Since they employ the l^1 norm of the control to keep the problem linear, they could recover a solution with higher propellant consumption if compared with the l^2 norm. To summarize, the state-of-the-art still lacks a method that can deal with an arbitrary number of conjunctions comprehensively (using TPoC) and does not need *a-priori* information on the maneuvering time. Moreover, all of the above-referenced works considered Keplerian dynamics, disregarding the contributions of orbital perturbations. Finally, to the best of the authors' knowledge, the multiple long-term conjunction CAM optimization problem has never been addressed.

An aspect that is closely related to this topic is the nonlinear propagation of the uncertainty in the state of the objects involved in the conjunctions. When the time span of the scenario involves multiple orbits and the uncertainties of the secondary spacecraft are discretely large, the initial Gaussian approximation can lose validity [20, 21]. We assume that accurate orbit determination is performed on the primary so that its uncertainty can be linearly propagated and remain Gaussian in the considered time window. Different methods can be used to recover an accurate description of the uncertainty of the secondary after a long propagation. Among these, the Monte Carlo analysis is the most accurate but most computationally expensive; unscented transforms reduce the computational load but assume Gaussian distribution, Gaussian mixture model (GMM) provide a good compromise between accuracy and computational load [22]. The research papers previously mentioned either do not consider the evolution of the uncertainty (because they use the instantaneous value of covariance given by a Conjunction Data Message (CDM)), or they only consider a linear propagation. In this regard, a first attempt at including the nonlinear propagation of the covariance matrix in the CAM optimization was taken by Dutta and Misra, who recently developed a pseudo-squared Mahalanobis distance (SMD) approach to treat a single conjunction with GMM [23]. This work will show how the approach developed for multiple conjunctions defined by CDMs can be adapted to treat multiple conjunctions where the initial covariance is propagated nonlinearly using a GMM. This allows for a more accurate depiction of the keep-out-zone (KOZ) when defining the convexified PoC constraint.

The solution methodology is based on convex optimization methods and is tailored to address the intricacies of multiple encounters and nonlinear uncertainty propagation. This direct optimization approach is chosen for its proven capability in solving complex aerospace engineering problems efficiently [24–26]. These findings highlight the convenience of employing a second-order cone program (SOCP) to formulate the convexified problem, as it allows for the minimization of the l^2 norm of the control history, which is a crucial requirement in spacecraft trajectory optimization problems. Turning the problem into an SOCP involves convexifying all non-convex aspects of the original optimal control problem (OCP), notably the fuel-optimal objective function, the nonlinear dynamics constraint, and the PoC constraint [27]. In the proposed approach, lossless relaxation is used to linearize the objective function. Furthermore, the nonlinear dynamics are automatically linearized using differential algebra (DA), which gives absolute freedom on

the dynamics model considered. The convexification approach proposed in reference [5] is used to linearize the PoC constraint in the short-term problem, and the one proposed in reference [18] is employed for the IPoC constraint in the long-term problem.

To enhance convergence, a trust region constraint, drawing from references [28–30], is employed to confine the solution space. However, due to the linearization of the dynamics, the optimizer cannot attain the optimal solution in a single SOCP run. Hence, a sequential convex program (SCP) is constructed as a sequence of SOCPs, where the solution from the previous iteration serves as the linearization point for the new iteration. This iterative process may necessitate a discrete number of iterations before converging to the optimal solution. Moreover, to account for the combined nature of TPoC between the multiple encounters, a third outer iteration process is used to find the optimal maneuver. This process automatically adapts the single PoC limits associated with the conjunctions. Alternatively, a single SCP run is performed where, in place of the method proposed in [5] and [18], a direct linearization of the PoC or IPoC constraint is used.

In the subsequent sections, the paper will present the proposed methodology’s mathematical framework and elaborate on the SCP approach for approximating the optimal control problem. Simulated case studies will demonstrate the approach’s effectiveness in generating fuel-efficient CAMs for multiple short- and long-term encounters. By addressing this increasingly pertinent challenge, this paper aims to offer a valuable contribution to the scope of spacecraft collision avoidance (CA) in cluttered orbital environments.

II. Formulation of the Collision Avoidance Problem

We consider multiple conjunctions between a primary spacecraft and $n_{conj} \in \mathbb{N}$ secondary objects. The primary is subject to a close encounter with each secondary at a certain time of closest approach (TCA), indicated with $t_{CA,s}$, where $s \in \{1, \dots, n_{conj}\}$. The primary and the secondary objects are characterized by a mean state and a covariance matrix at the starting time of the simulation t_0 or the conjunction’s TCA, $t_{CA,s}$. The states are represented using any arbitrary set of elements, e.g. Cartesian, Keplerian, or generalized equinoctial elements

$$\mathbf{x}_p(t_0) \sim \mathcal{N}(\boldsymbol{\zeta}_p(t_0), \mathbf{C}_p(t_0)), \quad \mathbf{x}_s(t_{CA,s}) \sim \mathcal{N}(\boldsymbol{\zeta}_s(t_{CA,s}), \mathbf{C}_s(t_{CA,s})) \quad \text{for } s \in \{1, \dots, n_{conj}\} \quad (1)$$

where $\mathbf{x}_p(t_0)$ and $\mathbf{x}_s(t_{CA,s}) \in \mathbb{R}^6$ are Gaussian multivariate random variable (MRV) variables, $\boldsymbol{\zeta}_p(t_0)$ and $\boldsymbol{\zeta}_s(t_{CA,s}) \in \mathbb{R}^6$ are the mean values, $\mathbf{C}_p(t_0)$ and $\mathbf{C}_s(t_{CA,s}) \in \mathbb{R}^{6 \times 6}$ are the covariance matrices.

The propagation of the state of the primary and the secondaries can be performed under a generic dynamical model

$$\dot{\mathbf{x}}_p(t) = \mathbf{f}_p(t, \mathbf{x}_p(t), \mathbf{u}(t), \mathbf{p}_p), \quad \dot{\mathbf{x}}_s(t) = \mathbf{f}_s(t, \mathbf{x}_s(t), \mathbf{p}_s) \quad \text{for } s \in \{1, \dots, n_{conj}\}, \quad (2)$$

where $t \in \mathbb{R}_{[t_0, t_f]}$ is the independent time variable, $\mathbf{x}_p(t), \mathbf{x}_s(t), \dot{\mathbf{x}}_p(t)$ and $\dot{\mathbf{x}}_s(t) \in \mathbb{R}^6$ are the time-dependent states of the primary and the secondaries and their derivatives, $\mathbf{u}(t) \in \mathbb{R}^3$ is the control action, $\mathbf{p}_p \in \mathbb{R}^{m_p}$ and $\mathbf{p}_s \in \mathbb{R}^{m_s}$ are vectors of parameters, $\mathbf{f}_p(\cdot) : \mathbb{R}_{[t_0, t_f]} \times \mathbb{R}^6 \times \mathbb{R}^3 \times \mathbb{R}^{m_p} \rightarrow \mathbb{R}^6$ and $\mathbf{f}_s(\cdot) : \mathbb{R}_{[t_0, t_f]} \times \mathbb{R}^6 \times \mathbb{R}^{m_s} \rightarrow \mathbb{R}^6$ are continuous functions..

To precisely establish the PoC constraint, it is crucial to explicitly express the relative position of the primary object w.r.t. to each secondary. If the state of the two objects is expressed in Cartesian Earth Centered Inertial (ECI) coordinates ($\mathbf{x}_p(t) = [\mathbf{r}_p(t); \mathbf{v}_p(t)]$), as it is the case in Section IV the relative position is the subtraction of the first three elements of the two normally distributed MRV

$$\Delta \mathbf{r}_s(t) = \mathbf{r}_p(t) - \mathbf{r}_s(t) \quad s \in \{1, \dots, n_{conj}\}, \quad (3)$$

Given that the subtraction is a linear transformation, the relative position is also normally distributed

$$\Delta \mathbf{r}_s(t) \sim \mathcal{N}(\boldsymbol{\mu}_p(t) - \boldsymbol{\mu}_s(t), \mathbf{P}_p(t) + \mathbf{P}_s(t)) \quad s \in \{1, \dots, n_{conj}\}, \quad (4)$$

The standard OCP in the continuous domain for the short-term conjunction CAM problem is stated as follows

$$\min_u \quad J = \int_{t_0}^{t_f} u(t) dt, \quad (5a)$$

$$\text{s.t.} \quad \dot{\mathbf{x}}_p = \mathbf{f}(t, \mathbf{x}_p(t), \mathbf{u}(t)), \quad (5b)$$

$$P_{TC}(t) \leq \bar{P}_{TC}, \quad (5c)$$

$$\mathbf{x}(t_0) = \mathbf{x}_0, \quad (5d)$$

$$u(t) = \sqrt{u_1(t)^2 + u_2(t)^2 + u_3(t)^2}, \quad (5e)$$

$$u(t) \leq u_{max}, \quad (5f)$$

where $P_{TC} \in \mathbb{R}(\cdot) : \mathbb{R} \rightarrow \mathbb{R}$ is the TPoC, which is monotonically increasing with time, and $\bar{P}_{TC} \in \mathbb{R}$ is the limit value imposed to the TPoC. In Problem (5), Eq. (5a) is the fuel minimization objective function, Eq. (5b) is the dynamics constraint, Eq. (5c) is the PoC constraint, Eq. (5d) is the initial state bound, Eq. (5e) is an auxiliary constraint to define the norm of the control, and Eq. (5f) is the bound on the maximum value of the control action. The collision probability can include n_{conj} conjunctions. Since CAMs typically involve a Δv on the order of magnitude of [mm/s] or [cm/s], the mass loss due to the maneuver is not considered in the equations of motion and the optimization problem [5].

A. Multiple Short-Term Conjunctions

Conjunctions can be categorized into two types: short-term and long-term. Short-term conjunctions, being more frequent, have received a more comprehensive investigation. In such instances, the relative velocity is notably high, resulting in near-instantaneous collisions. Consequently, the dynamics of the conjunction can be effectively approximated as linear without sacrificing accuracy, and the event is typically studied on the two-dimensional B-plane [4, 5, 31, 32].

In a scenario where n_{conj} consecutive conjunctions take place, the B-plane of a conjunction s is centered on the secondary object, the η axis is aligned with the direction of the relative velocity of the primary w.r.t. the secondary, and the $\xi\zeta$ plane is perpendicular to the relative velocity axis. Since TCA is the time when the miss distance is lowest, it follows that $\Delta\mathbf{r}_s(t_{CA,s}) \cdot \Delta\mathbf{v}_s(t_{CA,s}) = 0$ and thus the relative position lies on the $\xi\zeta$ plane. The following discussion assumes that all the uncertainty is concentrated around the secondary object, and all the mass is concentrated around the primary [31, 33]. In this way, the primary's state, which has to be optimized, can be treated as a deterministic variable.

The PoC of a single encounter is given by the integration of the Probability Density Function (PDF) of the relative position over the circle \mathbb{C}_{HBR} defined by the combined hard body radius (HBR) of the two spacecraft and centered in the primary

$$P_{C,s} = \frac{1}{(2\pi)\sqrt{\det(\mathbf{P}_{\mathcal{B}}(t_{CA,s}))}} \iint_{\mathbb{C}_{HBR}} \exp\left(-\frac{\Delta\mathbf{r}_{\mathcal{B}}^T(t_{CA,s})\mathbf{P}_{\mathcal{B}}^{-1}(t_{CA,s})\Delta\mathbf{r}_{\mathcal{B}}(t_{CA,s})}{2}\right) dA, \quad (6)$$

where $\Delta\mathbf{r}_{\mathcal{B}}(t_{CA,s}) \in \mathbb{R}^2$ $\mathbf{P}_{\mathcal{B}}(t_{CA,s}) \in \mathbb{R}^{2 \times 2}$ are the projection of the relative position mean value and covariance on the encounter B-plane at TCA. The argument of the exponential function is the SMD at TCA, $d_{m,s}^2$, divided by 2. Various approaches have been proposed to numerically solve this integral over the years; in this work, we will use Chan's method [34]. By employing a numerical inversion of Chan's formula [32], it is possible to get the SMD limit from a PoC limit for the conjunction ($d_m^2 = f(\bar{P}_C)$). Chan's PoC formula is generally preferred over others because of its accuracy and computational efficiency [35].

Assuming that the conjunctions are uncorrelated, the TPoC of the multiple encounter scenario is computed as the complement of the probability of not colliding with any object

$$P_{TC} = 1 - \prod_{s=1}^{n_{conj}} (1 - P_{C,s}), \quad (7a)$$

$$P_{TC} \approx \sum_{s=1}^{n_{conj}} P_{C,s}. \quad (7b)$$

In the hypothesis of small probabilities, it can be shown that the product in Eq. (7a) can be replaced by the summation in Eq. (7b). We will always use Eq. (7a) when computing the TPoC, but we will leverage the approximated formula Eq. (7b) to compute first guesses for the limits values of the PoC of the single conjunctions. One might assume that the hypothesis of uncorrelation is a strong one because the trajectory of the primary would be affected by a collision, thus

changing the PoC of the subsequent conjunctions. Nonetheless, as Frigm *et al.* highlight [8], from an operation point of view, "there is no reason to suppose that a close approach with a particular secondary is likely to promote a close approach with some other secondary."

B. Multiple Long-Term Conjunctions

Patera [11] demonstrates that when the relative trajectory of the primary spacecraft diverges significantly from a straight line within the combined covariance ellipsoid, the encounter qualifies as long-term, requiring the use of a distinct model for the computation of PoC. Despite numerous recent efforts to develop efficient methods for computing PoC in long-term encounters (references [36–39]), the presence of nonlinear relative trajectories within the combined uncertainty ellipsoid makes the risk quantification and, consequently, the design of long-term CAMs very complex. Quantitative thresholds to distinguish between the two types of conjunctions have been proposed. Among these, Chan's [40] states that conjunctions are short-term if the path of relative motion may be considered a straight line over a distance of 8 – 25 km with a deviation lower than 2 m; Dolado *et al.*'s [41], instead, identify conjunctions as short-term if the relative velocity at TCA is higher than 10 m/s. In recent literature, it has been shown that IPoC is a valuable alternative to PoC when addressing long term encounters [19, 33, 42–44]: in general, an increase in PoC is accompanied by a high value of IPoC, so controlling the evolution of IPoC allows to indirectly control the growth of PoC. For this reason, in agreement with a good portion of the state-of-the-art, we use IPoC as a risk metric rather than the more complex PoC when dealing with long-term encounters.

The integral of the IPoC at any time $t \in \mathbb{R}_{[t_0, t_f]}$ must be performed over the the three spatial dimensions

$$P_{IC,s}(t) = \frac{1}{(2\pi)^{3/2} \det(\mathbf{P}(t))^{1/2}} \iiint_{\mathbb{S}_{\text{HBR}}} \exp\left(-\frac{\Delta \mathbf{r}_s^T(t) \mathbf{P}_{rel,s}^{-1}(t) \Delta \mathbf{r}_s(t)}{2}\right) dV, \quad (8)$$

where both the relative position mean value $\Delta \mathbf{r}_s(t) \in \mathbb{R}^3$ and its covariance $\mathbf{P}_{rel,s}(t) \in \mathbb{R}^{3 \times 3}$ evolve in time. Multiple approaches have been proposed to solve this integral. We will consider one analogous to Alfriend's [31] for long-term encounters (its derivation can be found in [18]). Under the assumption of this method, i.e., the PDF of the relative position is considered constant inside the hard body sphere, IPoC has a direct dependence on SMD

$$P_{IC,s}(t) = \sqrt{\frac{2}{\pi \det(\mathbf{P}(t))}} \frac{R^3}{3} \exp\left(-\frac{d_{m,s}^2(t)}{2}\right). \quad (9)$$

In this case, the SMD is computed using the three-dimensional relative position variable. Analogously to Eq. (7a), the total instantaneous probability of collision (TIPOC) in a multiple long-term encounters scenario is given by the combination of the single uncorrelated conjunctions

$$P_{TIC}(t) = 1 - \prod_{s=1}^{n_{conj}} (1 - P_{IC,s}(t)) \approx \sum_{s=1}^{n_{conj}} P_{IC,s}(t), \quad (10)$$

Where the approximated equation is obtained using the same approximation of Eq. (7b).

C. Gaussian Mixture Model for Uncertainty Propagation

When dealing with multiple encounters with the same secondary or with a long-term conjunction, the time frame of interest can be very extended, spanning in the order of magnitude of the orbital periods. In the former case, the B-plane configuration depends on the propagated covariance, whereas in the latter, it is necessary to know the values of the elements of the covariance matrix of the relative position at every time to compute the IPoC from Eq. (9). If the propagation period is sufficiently long, the nonlinearities of the dynamics propagation become predominant, and the Gaussianity of the state is lost.

An effective way to recover a precise propagation of the uncertainty, which avails in the computation of the collision metrics, is the use of a GMM. Through this technique, the PDF of the secondary spacecraft is split into $n_{mix} \in 2\mathbb{N} + 1$ mixands. Each mixand is characterized by a mean value and a covariance matrix derived from the original distribution. The propagations of the mixands happen independently, and they are handled as different secondaries. The initial PDF split of the secondary's state yields

$$p[\mathbf{x}(t)] = \sum_{c=1}^{n_{mix}} \gamma_c p_g[\mathbf{x}(t); \boldsymbol{\mu}_c(t), \mathbf{P}_c(t)], \quad (11)$$

where $c \in \{1, \dots, n_{mix}\}$ indicates the single mixand, p is the PDF of the secondary object, p_g indicates the Gaussian PDF, and $\gamma_c \in \mathbb{R}$ are a set of weights such that $\sum_{c=1}^{n_{mix}} \gamma_c = 1$. It is assumed that most of the uncertainty is concentrated in the state of the secondary, so there is no need to split the state of the primary.

Vitaldev's uni-variate library method is used to perform the split [22]. Given the original PDF $p[\mathbf{x}(t)]$, the uni-variate splitting library is applied along the direction $\hat{\mathbf{a}}$

$$\boldsymbol{\mu}_c = \boldsymbol{\mu} + \mu_c \mathbf{S} \hat{\mathbf{a}}^*, \quad (12a)$$

$$\mathbf{P}_c = \mathbf{S} \left[\mathbf{I} + (\sigma_c^2 - 1) \hat{\mathbf{a}}^* \hat{\mathbf{a}}^{*T} \right] \mathbf{S}^T, \quad (12b)$$

where the matrix \mathbf{S} is the Cholesky decomposition of \mathbf{P} , μ_c and σ_c are from the uni-variate splitting library and $\hat{\mathbf{a}}^*$ is

$$\hat{\mathbf{a}}^* = \frac{\mathbf{S}^{-1} \hat{\mathbf{a}}}{\|\mathbf{S}^{-1} \hat{\mathbf{a}}\|_2}. \quad (13)$$

Once the split has been performed, n_{mix} fictitious secondary objects are defined at TCA, which can be treated

independently in the CA framework. Each of these objects encounters the primary spacecraft each of the conjunction times n_{conj} . The TPoC or TIPoC, then, is derived from Eq. (7a) or Eq. (10) with the introduction of a nested product function and the mixand weights

$$P_{TC} = 1 - \prod_{s=1}^{n_{conj}} \prod_{c=1}^{n_{mix}} (1 - \gamma_c P_{C,cs}) \approx \sum_{s=1}^{n_{conj}} \sum_{c=1}^{n_{mix}} (\gamma_c P_{C,cs}), \quad (14a)$$

$$P_{TIC}(t) = 1 - \prod_{s=1}^{n_{conj}} \prod_{c=1}^{n_{mix}} (1 - \gamma_c P_{IC,cs}(t)) \approx \sum_{s=1}^{n_{conj}} \sum_{c=1}^{n_{mix}} (\gamma_c P_{IC,cs}(t)), \quad (14b)$$

where $P_{C,cs}$ and $P_{IC,cs} \in \mathbb{R}$ are the PoC and IPoC of the c -th mixand in the s -th conjunction. The approximated equations are obtained using the same approximation of Eq. (7b). The splitting direction \hat{a} is arbitrary, but it determines how good an approximation the GMM provides w.r.t. the real distribution. Following works like Losacco's [29] and Vittaldev's [45], a good selection of the splitting direction depends both on the nonlinearity index (NLI) of the propagation and on the components of the initial covariance matrix. The NLI, indicated with ν , gives a quantitative indication of the effect of the nonlinearities in a certain direction; in reference [29], how to compute it is effectively shown. A vector $\phi \in \mathbb{R}^6$ made of the 2-norm of each column of the initial covariance matrix is used to quantify the entity of the uncertainty in each direction

$$\phi_k = \sqrt{\sum_{l=1}^6 P_{lk}^2} \quad k \in [1, 6], \quad (15)$$

The splitting direction, then, considers the information from both the NLI and the covariance

$$\hat{a} = \frac{\nu \circ \phi}{\|\nu\| \cdot \|\phi\|}, \quad (16)$$

where \circ indicates the Hadamard product.

III. Convex Formulation

The OCP Problem 5 is transformed into a SCP to be solved iteratively. The methods applied are described in detail in [19]: the SCP iteratively approximates the global solution of the OCP via a sequence of SOCPs. Here, we recall the constraints and the objective function and adapt it to the multiple encounters problem. Three sources of non-convexities are present in the original OCP as formulated in Problem 5:

- 1) orbital dynamics in Eq. (5b) are highly nonlinear, thus non-convex.
- 2) Eq. (5c) is a nonlinear constraint because it involves the use of Eq. (7a) and the inversion of Chan's formula for short-term encounters or Eq. (9) for long-term ones.
- 3) Eq. (5a) and Eq. (5e) yield a nonlinear objective function.

These issues are addressed in the following sections, where the dynamics constraint, the PoC constraint, and the objective function are convexified using different techniques. A more detailed explanation of the convexification approach can be found in [5] and [19].

A. Convexification of the dynamics

The dynamics of the problem are first discretized and then automatically linearized using DA.

1. Discretization of the Dynamics

The continuous time variable $t \in \mathbb{R}_{[t_0, t_f]}$ is substituted by the discrete time variable $t_i \in \{t_0, t_1, \dots, t_N\}$, where $N + 1$ is the number of nodes of the discretization. Following Eq. (2) and via the use of an integration scheme, like Runge-Kutta 7-8, one obtains the states of the two spacecraft at node $i + 1$, which depend on the state and the control at node i :

$$\mathbf{x}_{p,i+1} = \mathbf{f}_{p,i}(t_i, \mathbf{x}_{p,i}, \mathbf{u}_i, \mathbf{p}_p) \quad i \in \{0, \dots, N - 1\}, \quad (17a)$$

$$\mathbf{x}_{s,i+1} = \mathbf{f}_{s,i}(t_i, \mathbf{x}_{s,i}, \mathbf{p}_s) \quad i \in \{0, \dots, N - 1\} \quad s \in \{1, \dots, n_{conj}\}, \quad (17b)$$

where $\mathbf{f}_{p,i}(\cdot) : \mathbb{R}_{[t_0, t_f]} \times \mathbb{R}^6 \times \mathbb{R}^3 \times \mathbb{R}^{m_p} \rightarrow \mathbb{R}^6$ and $\mathbf{f}_{s,i}(\cdot) : \mathbb{R}_{[t_0, t_f]} \times \mathbb{R}^6 \times \mathbb{R}^{m_s} \rightarrow \mathbb{R}^6$ are the functions that describe the dynamics at node i , $\mathbf{x}_{p,i} = \mathbf{x}_p(t_i)$, $\mathbf{x}_{s,i} = \mathbf{x}_s(t_i)$ and $\mathbf{u}_i = \mathbf{u}(t_i)$. The DA tool is used to introduce perturbations on the primary state ($\mathbf{x}_{p,i} + \delta\mathbf{x}_{p,i}$) and acceleration ($\mathbf{u}_i + \delta\mathbf{u}_i$) at each node, effectively expressing Eq. (17a) through Taylor polynomials:

$$\mathbf{x}_{p,i+1} = \mathcal{T}_{\mathbf{x}_{p,i+1}}^q(\mathbf{x}_{p,i}, \mathbf{u}_i) \quad i \in \{0, \dots, N - 1\}, \quad (18)$$

where in general the expression $\mathcal{T}_y^q(x)$ indicates the q^{th} -order Taylor expansion of the variable y as a function of x , around the expansion point \tilde{x} in which the polynomial is computed. The reader can find a detailed explanation of the use of DA in [46].

2. Linearization of the Dynamics

The discretized dynamics are linearized around a reference trajectory, so that a linear constraint can be set in the SOCP. This is an iterative process which can require numerous runs, referred to as major iterations and denoted by index j . Once the optimization problem of a major iteration $j - 1$ is solved, the solution $(\mathbf{x}^{j-1}, \mathbf{u}^{j-1})$ becomes available, a column vector comprising the state and control at each node. Employing DA, this solution serves as an expansion point for constructing linear dynamics maps for iteration j . The continuity condition is enforced by requiring that the state after the propagation of node i is equal to the state before the propagation of node $i + 1$. The state and acceleration of each node are expanded around the reference points, which are the output of the previous major iteration $\tilde{\mathbf{x}}_i^j = \mathbf{x}_i^{j-1}$

and $\tilde{\mathbf{u}}_i^j = \mathbf{u}_i^{j-1}$

$$\mathbf{x}_i^j = \tilde{\mathbf{x}}_i^j + \delta \mathbf{x}_i^j, \quad \mathbf{u}_i^j = \tilde{\mathbf{u}}_i^j + \delta \mathbf{u}_i^j \quad i \in \{0, \dots, N-1\}, \quad (19)$$

The state at the subsequent node is obtained through the propagation of the first-order dynamics. The linear continuity constraint imposes that the linearly propagated state be equal to the state at the subsequent node

$$\mathbf{x}_{i+1}^j = \mathbf{A}_{i+1}^j \mathbf{x}_i^j + \mathbf{B}_{i+1}^j \mathbf{u}_i^j + \mathbf{c}_i^j \quad i \in \{0, \dots, N-1\}, \quad (20)$$

where $\mathbf{A}_{i+1}^j \in \mathbb{R}^{6 \times 6}$ is the state transition matrix, $\mathbf{B}_{i+1}^j \in \mathbb{R}^{6 \times 3}$ is the control-state transition matrix, $\mathbf{c}_i^j = \bar{\mathbf{x}}_{i+1} - \mathbf{A}_{i+1}^j \tilde{\mathbf{x}}_i^j - \mathbf{B}_{i+1}^j \tilde{\mathbf{u}}_i^j$ is the residual of the linearization, and $\bar{\mathbf{x}}_{i+1} = \mathbf{f}_{p,i}(t_i, \tilde{\mathbf{x}}_i, \tilde{\mathbf{u}}_i)$ is the constant part of the propagation of the state. The initial condition is fixed because the maneuver cannot alter it

$$\mathbf{x}_0^j = \mathbf{x}_0^0. \quad (21)$$

3. Lossless Relaxation of the Control Magnitude Constraint

Equation Eq. (5e) is a non-convex equality constraint. Following the work from [47], we introduce a lossless relaxation to convexify the constraint: Eq. (5e) is transformed into an inequality constraint, and the control magnitude is added to the optimization vector. In this way, Eq. (5e) becomes a second-order cone constraint. The variable u_i is now allowed to take values higher than the norm of the control that acts on the dynamics

$$u_i \geq \sqrt{u_{i,1}^2 + u_{i,2}^2 + u_{i,3}^2} \quad i \in \{0, \dots, N-1\}. \quad (22)$$

The discretized forms of Eq. (5a) and Eq. (5f) become respectively

$$J = \sum_{i=0}^{N-1} u_i \cdot \Delta t_i, \quad (23)$$

$$0 \leq u_i \leq 1 \quad i \in \{0, \dots, N-1\}, \quad (24)$$

where $\Delta t_i = t_{i+1} - t_i$ is the time for which the control is active from node i to $i+1$. This linearization of the objective function is lossless, meaning that the optimal solution for the convexified problem is also optimal for the original problem.

4. Trust region approach

Using a trust region constraint in formulating the SOCP is greatly beneficial for the convergence of the algorithm [28]. In this work, the approach originally introduced in [30] and adapted in [19] is used, which is reliant on the definition of the NLI from [29]. The interested reader is invited to refer to these works for details on the derivation of the constraint. The gist of the approach is to consider the radius of the trust region of an optimization variable as inversely proportional to its nonlinearity. The resulting constraints are

$$\xi_i \circ [\mathbf{x}_i^T; \mathbf{u}_i^T]^T \leq \xi_i \circ [\tilde{\mathbf{x}}_i^T; \tilde{\mathbf{u}}_i^T]^T + \bar{\nu} \cdot \mathbf{1} \quad i \in \{1, \dots, N\}, \quad (25a)$$

$$\xi_i \circ [\mathbf{x}_i^T; \mathbf{u}_i^T]^T \geq \xi_i \circ [\tilde{\mathbf{x}}_i^T; \tilde{\mathbf{u}}_i^T]^T - \bar{\nu} \cdot \mathbf{1} \quad i \in \{1, \dots, N\}, \quad (25b)$$

where ξ_i is the measure of the nonlinearity of the associated state vector in the second-order DA propagation of the dynamics [30]; $\bar{\nu}$ is a user-defined value that imposes a limit to the maximum NLI available to the solution.

The introduction of the trust region constraint can cause artificial infeasibility, so virtual controls are added to the dynamics constraints, Eq. (20). The new constraints with virtual controls become

$$\mathbf{x}_{i+1}^j - \mathbf{A}_{i+1} \mathbf{x}_i^j - \mathbf{B}_{i+1}^j \mathbf{u}_i^j + \mathbf{v}_{i+1}^j - \mathbf{c}_i^j = 0 \quad i \in \{0, \dots, N-1\}, \quad (26)$$

where $\mathbf{v}_i^j \in \mathbb{R}^6$ is the virtual control vector for the node i at major iteration j .

In the objective function, a term is added which is proportional to the entity of the virtual controls in order to minimize them. This term is multiplied by a weight $\kappa_{vc} \in \mathbb{R}$, which must be sufficiently high.

$$v_i \geq \|(v_{ca,i}^j)\| \quad i \in \{1, \dots, N\}, \quad (27a)$$

$$J_{vc} = \kappa_{vc} \sum_{i=0}^N v_i, \quad (27b)$$

B. Convexification of the PoC Constraint for Short-Term Encounters

Two alternative approaches are proposed to convexify the PoC constraint. The first one is based on the linearization of the SMD, and it consists of setting a separate constraint for each conjunction; the second is based on a direct linearization of the TPoC formula of Eq. (7a).

1. Linearized SMD constraint

The PoC constraint for a single conjunction can be formulated by leveraging the methodology proposed in references [48] and [5]. The reader is invited to refer to this last reference for an in-depth explanation of the process. An iterative

projection and linearization algorithm is utilized to convexify the nonlinear PoC constraint. The iterations are nested inside the major iterations used to linearize the dynamics and take the name of *minor iterations*, denoted by the symbol k . For each conjunction node, the projection convex sub-problem aims to find the point on the surface of an ellipse that is closest to the relative position $\Delta \mathbf{r}_s^{j,k-1}$ from the previous minor iteration (where $s \in \{1, \dots, n_{conj}\}$). In the formulation of the convex sub-problem, the indices s and j are dropped since one of these problems is solved multiple times inside the same major iteration and for each conjunction.

Let the covariance and relative position be expressed in the B-plane reference frame \mathcal{B} . It is possible to define a transformation matrix $\mathbf{V} \in \mathbb{R}^2$ that diagonalizes the covariance matrix. We call the reference frame in which the covariance matrix is diagonal \mathcal{C} . A simple quadratic optimization problem is used to find the point on the ellipse that is closest to the reference trajectory point

$$\min_{\mathbf{z}_C} \|\mathbf{z}_C^k - \Delta \mathbf{r}_{q,C}^{k-1}\| \quad (28a)$$

$$\text{s.t. } (\mathbf{z}_C^k)^T (\mathbf{P}_C)^{-1} \mathbf{z}_C^k \leq \bar{d}_m^2, \quad (28b)$$

The objective Eq. (28a) imposes the minimization of the Euclidean distance between the relative position of the previous iteration and the optimization variable \mathbf{z}_C . Eq. (28b) is a relaxed condition on the optimization variable to be inside the ellipsoid. These relaxed conditions are lossless since the minimization of the objective guarantees that the optimized variable is always positioned on the ellipse's surface, maximizing the distance from its center.

Once \mathbf{z}_C is determined, the solution is transformed back into the original reference frame using the equation $\mathbf{z}_B^k = \mathbf{V}^T \mathbf{z}_C^k$. After obtaining $\mathbf{z}_s^{j,k} = \mathbf{z}_B^k$, a linearization of the SMD constraint is applied, effectively turning it into a KOZ constraint. Specifically, we ensure that the new optimized relative position lies within the semi-plane defined by the line tangent to the ellipse on $\mathbf{z}_s^{j,k}$. The equation of the constraint is, then

$$\nabla (d_m^2)_s^{j,k} \Big|_{\mathbf{z}_s^{j,k}} \cdot (\Delta \mathbf{r}_i^{j,k} - \mathbf{z}_s^{j,k}) \geq 0 \quad i \in \{1, \dots, N\}. \quad (29)$$

2. Linearized TPoC constraint

An alternative to the use of the linearized SMD constraint is the linearized TPoC constraint. The formula of the TPoC from Eq. (7a) is linearized using DA as a function of the relative position in each of the encounters

$$\delta P_{TC} = \nabla \delta \mathbf{r}, \quad (30)$$

where ∇ is the gradient of the expression that gives the total PoC as a function of the relative position at each TCA and \mathbf{r} is the stacked vector of the positions of the primary in the nodes in which the conjunctions happen, i.e., the TCAs

$$\mathbf{r} = \begin{bmatrix} \mathbf{r}_1^T & \dots & \mathbf{r}_{n_{conj}}^T \end{bmatrix}^T \quad (31)$$

The PoC constraint, in this case, is a scalar one

$$P_{TC} = \nabla \mathbf{r} + d \leq \bar{P}_{TC}, \quad (32)$$

where $d = \bar{P}_{TC} - \nabla \tilde{\mathbf{r}}$ is the residual of the linearization (the tilde indicates the values computed at the expansion point). Note that using the absolute or the relative position of the primary is equivalent because in Eq. (32), the position of the secondary would be eliminated. A trust region constraint is used to favor the convergence of the optimization with this constraint.

The trust region method is analogous to the one used to impose a trust region constraint based on the dynamics in [19]. Eq. (7a) is computed using a second-order DA expansion, which yields the gradient of the function with a first order-expansion

$$\nabla = \bar{\nabla} + \delta \nabla, \quad (33)$$

where $\bar{\nabla} \in \mathbb{R}^{3n_{conj}}$ is the constant part of the gradient and $\delta \nabla \in \mathbb{R}^{3n_{conj}}$ is its first-order expansion w.r.t. the position vector.

$$\nabla_i = \bar{\nabla}_i + \delta \nabla_i = \bar{\nabla}_i + \sum_{j=1}^{3n_{conj}} a_{ij} \delta r_j \quad i \in \{1, \dots, 3n_{conj}\} \quad (34)$$

The non-linearity vector for the single relative position variable r_j is computed as the ratio between the norm of the second-order terms and that of the first-order ones

$$\nu_j = \frac{\sqrt{\sum_{i=1}^{3n_{conj}} a_{ij}^2}}{\|\bar{\nabla}\|} |\delta r_j| = \xi_j |\delta r_j|. \quad (35)$$

It is possible to write two vector equations for each conjunction, which bound the position of the given node

$$\xi_k \circ \Delta \mathbf{r}_k \leq \xi_k \circ \Delta \tilde{\mathbf{r}}_k + \boldsymbol{\nu} \quad k \in \{1, \dots, n_{conj}\}, \quad (36a)$$

$$\xi_k \circ \Delta \mathbf{r}_k \geq \xi_k \circ \Delta \tilde{\mathbf{r}}_k - \boldsymbol{\nu} \quad k \in \{1, \dots, n_{conj}\}, \quad (36b)$$

where ξ_k and $\boldsymbol{\nu}_k \in \mathbb{R}^3$ include the three components of the single encounter.

3. Refinement of the solution

The PoC constraint of the original OCP Eq. (5c) bound the TPoC to below a limit value \bar{P}_{TC} . This limit can be split, and a portion of it can be assigned to the single conjunctions

$$\bar{P}_{TC} = 1 - \prod_{s=1}^{n_{conj}} (1 - \bar{P}_{C,s}). \quad (37)$$

Theoretically, in Eq. (37), the single limits $\bar{P}_{C,s}$ can be optimized to build constraints that allow for the minimization of the Δv . Under the assumption that a higher Δv leads to a lower TPoC, we need to find a method to recover a solution for which the final TPoC gets as close as possible to the total limit.

A first SCP is solved using a first guess for the limits of the single conjunctions. They are all set to the same value by leveraging the approximated Eq. (7b)

$$\bar{P}_{C,s} = \frac{\bar{P}_{TC}}{n_{conj}} \quad s \in \{1, \dots, n_{conj}\}, \quad (38)$$

so that Eq. (37) is automatically satisfied. This first convex run's total PoC is typically much lower than \bar{P}_{TC} , so a refinement is executed. We have two alternatives for the PoC constraint of this second SCP, which are reported schematically in Fig. 1. The first option is to include the linearized TPoC constraint on the right side of Fig. 1. In fact, since it is based on a heavy linearization of the PoC formula, it is unlikely to converge when a good reference solution is not provided, and it can only be used to refine the solution obtained with the first convex run. An alternative approach, reported in the left side of Fig. 1, consists of adapting the limit PoC values $\bar{P}_{C,s}$ and running a new SCP with the new optimized values.

To tune the limit of each conjunction to optimal values, a non-linear program (NLP) is solved. In Fig. 2, the purpose of the NLP is shown. The PoC limits imposed in the first SCP yield SMD limits that identify the dashed ellipses. Given these two limits, the convex solver may find a solution like the blue dots: the first conjunction dominates the scenario because r_1^0 is on the border of the ellipse, while r_2^0 is far from it. After the limits adaptation, more importance is given to the first conjunction. The limit PoC of the first conjunction is increased so that its SMD limit decreases, and the solution to the new SCP might be found closer to the ballistic miss distance. The minimization of the miss distance of the second conjunction is of no concern because, in the first run, the optimized point was found far from the limit. So, the SMD threshold of the second is allowed to grow (or the PoC threshold to shrink) until it reaches a value for which the optimized point is on the limit.

The optimization variables of the NLP are collected in two vectors of parameters, α and $\rho \in \mathbb{R}^{n_{conj}}$. α is such that for the s -th conjunction $\bar{P}_{C,s} = \bar{P}_{TC} \cdot 10^{-\alpha_s}$. We choose to introduce this parameter as an exponent to favor the algorithm's convergence since the limit PoC values can span a wide range of orders of magnitude; the minus sign of the

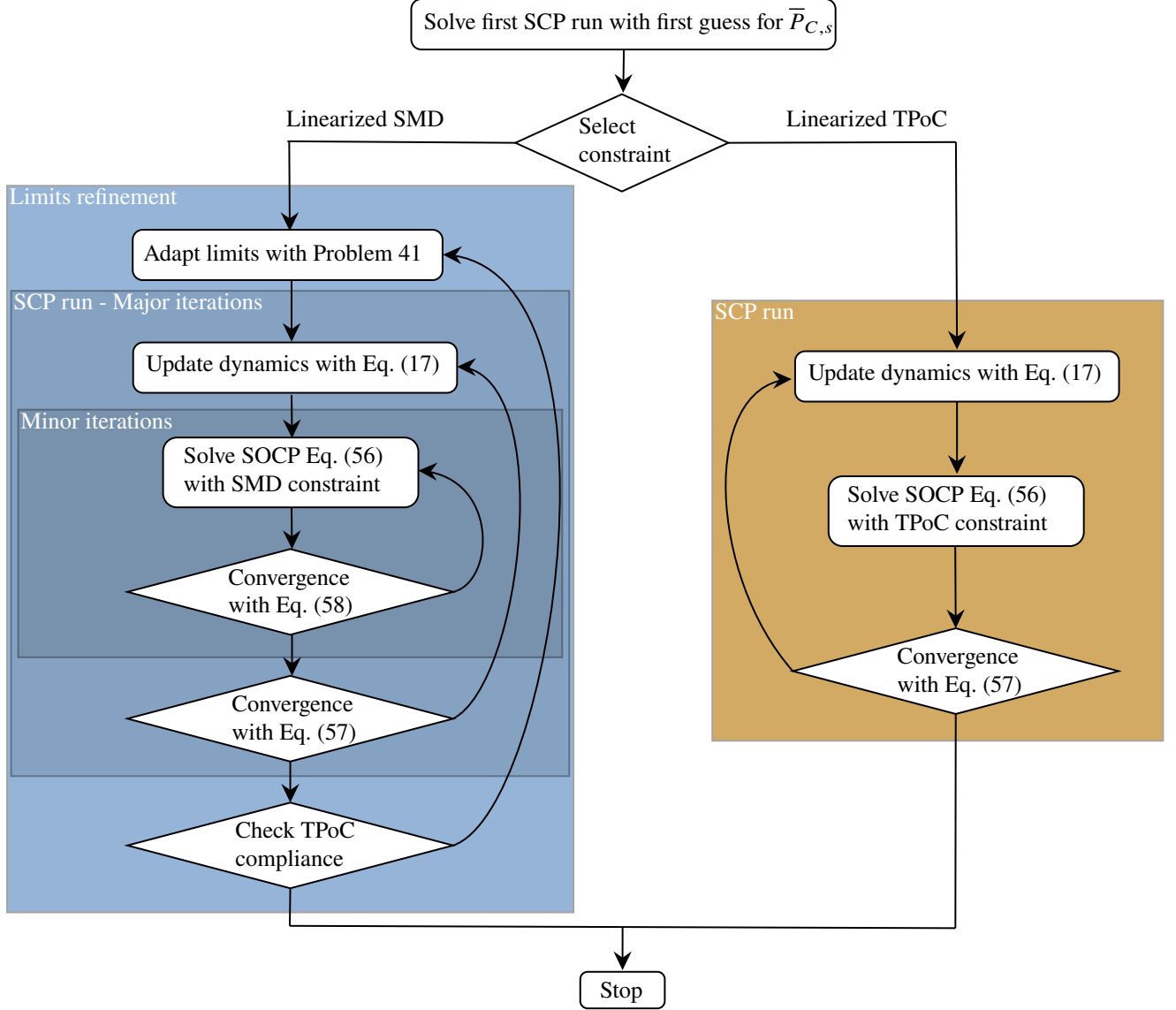


Figure 1 High-level flow of the algorithm.

exponent is useful to keep the optimization variables always positive. Our working hypothesis affirms that getting closer to the ballistic relative position would result in a lower Δv . So, the optimized relative position is bound to lie in the same direction as the point resulted from the previous SCP w.r.t. the ballistic relative position.

$$\Delta \hat{\mathbf{r}}_s = \frac{\Delta \mathbf{r}_s^0 - \Delta \mathbf{r}_s^{ball}}{\|\Delta \mathbf{r}_s^0 - \Delta \mathbf{r}_s^{ball}\|}, \quad (39)$$

where $\Delta \mathbf{r}_s^0$ and $\Delta \mathbf{r}_s^{ball} \in \mathbb{R}^3$ are the relative position of the previous SCP run and of the ballistic trajectory w.r.t. the secondary s . In this way, we only need to optimize the magnitude of the difference between the optimized relative

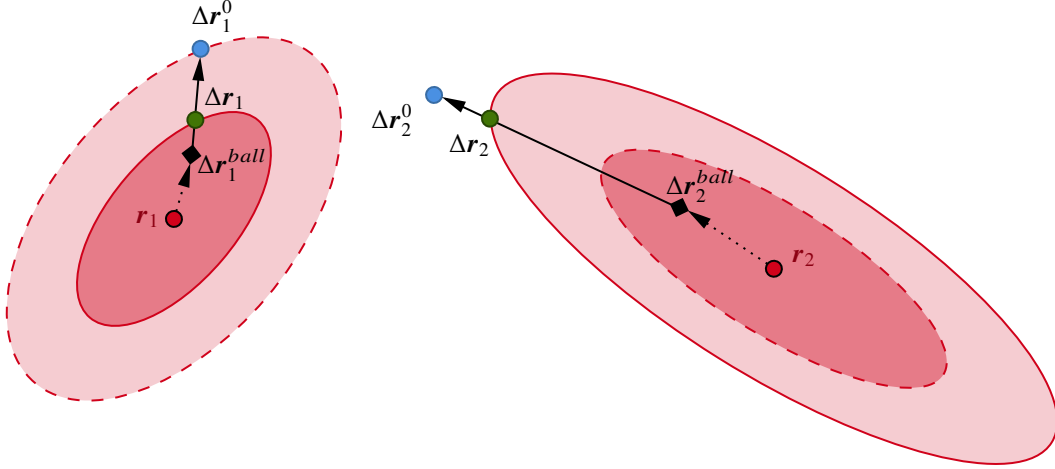


Figure 2 Scheme of the adaptation of the PoC limits for two conjunctions.

position and the ballistic one (ρ_s) for each conjunction s

$$\rho_s = \|\Delta \mathbf{r}_s - \Delta \mathbf{r}_s^{ball}\| \quad s \in \{1, \dots, n_{conj}\}. \quad (40)$$

$\boldsymbol{\rho}$ collects the ρ_s for every conjunction. Now we can write the NLP that is used to optimize the limit probabilities. In Problem 41, the variables with superscript 0 indicate the output of the previous SCP

$$\min_{\boldsymbol{\rho}, \boldsymbol{\alpha}} \quad \boldsymbol{\rho} \cdot \boldsymbol{\beta} \quad (41a)$$

$$\text{s.t.} \quad \Delta \mathbf{r}_s = \Delta \mathbf{r}_s^{ball} + \rho_s \Delta \hat{\mathbf{f}}_s \quad s \in \{1, \dots, n_{conj}\}, \quad (41b)$$

$$\bar{P}_{C,s} = \bar{P}_{TC} \cdot 10^{-\alpha_s} \quad s \in \{1, \dots, n_{conj}\}, \quad (41c)$$

$$P_{C,s}(\Delta \mathbf{r}_s, \mathbf{P}_s, HBR_s) \leq \bar{P}_{C,s} \quad s \in \{1, \dots, n_{conj}\}, \quad (41d)$$

$$1 - \bar{P}_{TC} - \prod_{s=1}^{n_{conj}} (1 - \bar{P}_{C,s}) = 0, \quad (41e)$$

$$\beta_s = \begin{cases} 1 & \text{if } |P_{C,s}^0 - \bar{P}_{C,s}^0| / \bar{P}_{C,s}^0 \leq \varepsilon \\ 0 & \text{otherwise} \end{cases} \quad s \in \{1, \dots, n_{conj}\}, \quad (41f)$$

$$0 \leq \rho_s \leq \rho_s^0 \quad s \in \{1, \dots, n_{conj}\}, \quad (41g)$$

$$0 \leq \alpha_s \leq 10 \quad s \in \{1, \dots, n_{conj}\}. \quad (41h)$$

The objective function in Eq. (41a) is the norm of the scaled distance of the optimized point from the ballistic one. With

Eq. (41b), the optimized point is bound to lie in the same direction as the point resulted from the previous SCP w.r.t. the ballistic relative position. Eq. (41c) defines the PoC limits as functions of the optimization variable α . Eq. (41d) sets the collision avoidance constraint for each secondary. Eq. (41e) imposes that the combination of the PoC limits must give the TPoC limit. In Eq. (41f), the vector $\beta \in \mathbb{R}^{n_{conj}}$ is used to ensure that the conjunctions that affect the objective function are the ones for which the PoC contributes in a non-negligible manner to the TPoC; $\varepsilon \in \mathbb{R}$ is a tolerance value, e.g., 10^{-2} . The last two constraints, Eq. (41g) and Eq. (41h), are bound constraints on the optimization variables.

As a solution of Problem 41, one obtains the weights in α that are used to find the limit PoC for each conjunction. Using this objective function requires the underlying hypothesis that a solution to the convex problem that is closer to the original ballistic trajectory would require a lower Δv , which might not always be the case. Lastly, it is important to feed the NLP a suitable first guess in terms of α_0 and ρ_0 : the value of ρ_0 is taken from the result of the previous SCP, and α_0 is derived from the values of the PoC associated with the single conjunctions

$$\alpha_{0,s} = -\log\left(\frac{P_{C,s}^0}{\bar{P}_{TC}}\right) \quad s \in \{1, \dots, n_{conj}\}. \quad (42)$$

C. Conjunction representation with GMM

The GMM representation of the uncertainty can be used in the framework of the multiple encounters with just a few adjustments. It is easy to visualize every mixand as a separate secondary, thus treating the conjunctions separately, like in the scenario where multiple encounters happen with different objects. As shown in Fig. 3, depending on the direction of the split and on the direction of relative motion between the two bodies, the TCAs of the different mixands can be very close, if not identical. This is equivalent to the primary being required to avoid the collision with more than two very close objects at times that are close to one another. The issue arises of the previously established time grid (on which the dynamics have been discretized) not being able to catch the exact TCAs. This calls for refining the grid near the nominal TCA. Fig. 4 depicts the idea of the grid refinement for a case with three mixands: the original equally spaced time grid is represented in black. While for the first conjunction, in this particular case, the three mixands all arrive at the close approach at the same time, for the second conjunction, they have had the time to drift from each other; thus, the close encounter with the primary happens at the nominal time for the central mixand (dark green line) and at slightly different times for the other two (light green lines). A grid thickening algorithm is used to be able to catch the offset TCAs, yielding new nodes like the ones represented in red.

First of all, the real TCA must be computed. One could do this by propagating the trajectory from node $t_{CA,s}$ previous to the TCA one and the one subsequent to it and finding the time for which the minimum separation is reached. This method, though, is highly inefficient. We leverage DA to obtain the same result. For a conjunction

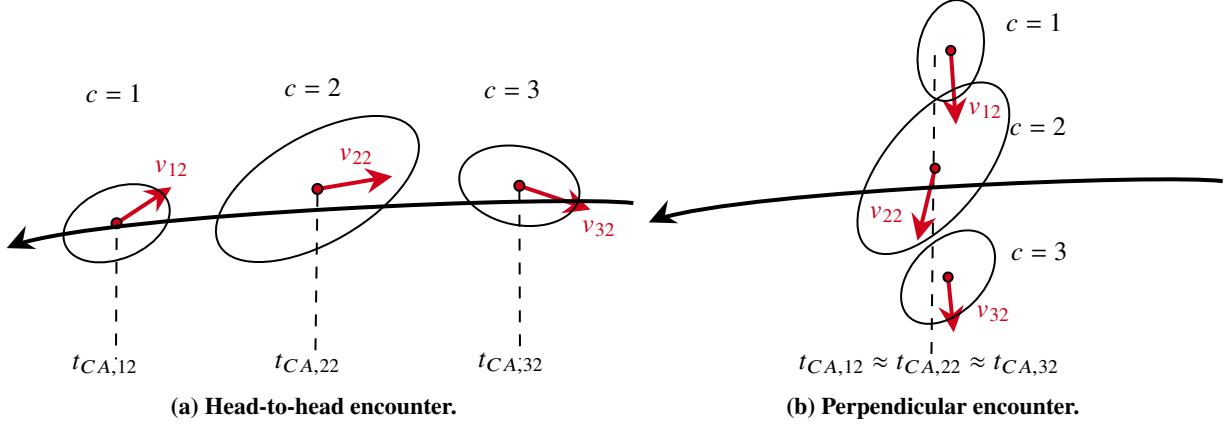


Figure 3 Different geometric configurations of the conjunctions depending on the direction of relative motion.

$s \in \{1, \dots, n_{conj}\}$, let us take the nominal states of the two spacecraft at TCA and expand the secondary state

$$\mathbf{x}_{s,CA}^j = \tilde{\mathbf{x}}_{s,CA}^j + \delta \mathbf{x}_{s,CA}^j, \quad (43)$$

We propagate the states of the two satellites by a DA variable δt_s , obtaining, with a Taylor polynomial notation

$$\mathbf{x}_{s,CA}^{j*} = \mathcal{T}_{\mathbf{x}_{s,CA}^j}^1(\delta t_s, \delta \mathbf{x}_{s,CA}^j), \quad \mathbf{x}_{p,CA}^{j*} = \mathcal{T}_{\mathbf{x}_{p,CA}^{j*}}^1(\delta t_s), \quad (44)$$

where the stars indicate the variables at the real TCA. The relative state is a new Taylor polynomial dependent on $\mathbf{x}_{s,CA}^j$, $\tilde{\mathbf{x}}_{p,CA}^j$ and δt_s : $\Delta \mathbf{x}_{s,CA}^{j*} = \mathbf{x}_{p,CA}^{j*} - \mathbf{x}_{s,CA}^{j*}$. It can be split into the position and velocity parts to write the equation of the minimum distance. As mentioned in Section III.B, the relative position is minimum when the relative velocity is orthogonal to it

$$\Delta \mathbf{r}_{CA}^* \cdot \Delta \mathbf{v}_{CA}^* = \mathcal{T}_{\Delta \mathbf{r}_{CA}^* \cdot \Delta \mathbf{v}_{CA}^*}^1(\delta t_s, \delta \mathbf{x}_{s,CA}^j) = 0. \quad (45)$$

This parametric implicit equation can be solved for δt_s using a polynomial partial inversion technique, as the one used in [46] and [49]. The equation for δt_s reads

$$\delta t_s = \mathcal{T}_{\delta t_s}^1(\Delta \mathbf{r}_{CA}^* \cdot \Delta \mathbf{v}_{CA}^*, \delta \mathbf{x}_{s,CA}^j). \quad (46)$$

The exact TCA of the single mixand, then, is

$$t_{CA,s}^* = t_{CA,s} + \delta t_s. \quad (47)$$

According to the new TCAs, nodes are added to the time grid, and the states of the primary and the relevant mixands are

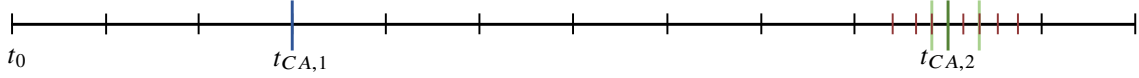


Figure 4 Grid adjustment to account for different TCAs of the mixands.

propagated to such times.

If a GMM model is used to propagate the uncertainty, we can treat each mixand as an independent secondary object. This way, we can navigate back to the algorithm described in the previous section. If we want to adapt the limits of the mixands to refine the solution, we can use Problem 41, with two slight differences. Firstly, in the first guess, we use the approximated version of Eq. (14a) and the limits are set proportional to the weights

$$\bar{P}_{C,cs} = \frac{\gamma_c}{n_{conj}} \bar{P}_{TC} \quad c \in \{1, \dots, n_{mix}\} \quad s \in \{1, \dots, n_{conj}\}, \quad (48)$$

where n_{mix} is the number of GMM mixands, s indicates the conjunction and c indicates the mixand; this is not a necessary condition since any combination of thresholds is valid as long as it respects the total probability threshold, but it is found to favor convergence in practice.* Secondly, in Eq. (41d), the PoC of the conjunction obtained with Chan's formulas must be multiplied by its weight

$$\gamma_c P_{C,cs}(\mathbf{r}_{cs}, \mathbf{C}_{cs}, HBR_s) \leq \bar{P}_{C,cs} \quad c \in \{1, \dots, n_{mix}\} \quad s \in \{1, \dots, n_{conj}\}, \quad (49)$$

and in Eq. (41e), the nested product must be included to account for the GMM components in each conjunction

$$1 - \bar{P}_{TC} - \prod_{s=1}^{n_{conj}} \prod_{c=1}^{n_{mix}} (1 - \bar{P}_{C,cs}) = 0. \quad (50)$$

If Eq. (48) is substituted into Eq. (50) we see that the total limit is respected by the initial arbitrary split.

One last remark about the optimization with the GMM method regards the computation of the SMD limit. To obtain a realistic SMD limit from the PoC limit with the inversion of Chan's formula, the mixand weight must be taken into account

$$\bar{d}_{m,cs}^2 = f\left(\frac{\bar{P}_{C,cs}}{\gamma_c}\right) \quad c \in \{1, \dots, n_{mix}\} \quad s \in \{1, \dots, n_{conj}\}. \quad (51)$$

D. Convexification of the PoC Constraint for Long-Term Encounters

When dealing with the long-term encounter problem, the adopted approach is derived from the one described in the previous Section III.B, with some substantial differences presented in this section. A detailed description of the

*For example, the equation $\bar{P}_{C,cs} = \bar{P}_{TC} / (n_{mix} \cdot n_{conj})$ would be equally valid.

projection and linearization algorithm for the single conjunction in long-term encounters is given in reference [19]. Here, it suffices to say that it is analogous to the one presented in Section III.B.1, but instead of working in the B-plane, we set the problem in the 3D ECI reference frame. There is no particular need to use an ECI frame, but it is convenient because it does not require transformations with respect to the frame used for the propagation of the dynamics.

1. Linearized TIPoC Constraint

A similar approach to Section III.B.2 is used for the TIPoC constraint in the case of long-term encounters. In this case, the constraint has to be applied indistinctly at every node of the optimization, so the stack of positions changes node-wise $\mathbf{r} \in \mathbb{R}^{3n_{conj} \times N}$ and so does the Jacobian $\mathbf{J} \in \mathbb{R}^{3n_{conj} \times N}$. The node-wise linearized TIPoC constraint reads

$$P_{TIC,i} = \nabla_i \mathbf{r}_i + d_i \leq \bar{P}_{TIC}, \quad i = \{1, \dots, N\} \quad (52)$$

where $\nabla_i \in \mathbb{R}^{3n_{conj}}$ is the gradient of the expression that gives the TIPoC as a function of the relative position w.r.t. each secondary and $d = \bar{P}_{TIC,i} - \nabla_i \mathbf{r}_i$ is the residual of the linearization. The same trust region method from Section III.B.2 is employed, bearing in mind that, in this case, the trust region must be applied to the relative position variables at each node of the optimization.

2. Refinement of the solution

When dealing with multiple secondaries or propagating GMM components, also in long-term encounters, it is important to refine the solution with one of the two methods introduced in Section III.B.3. The first one, based on the linearization of the TIPoC, was shown in Section III.D.1. The second one consists of adapting the IPoC threshold of each component to obtain the minimum Δv maneuver. An analogous NLP to the one presented in Problem 41 is used to tune the weights of the limits after the problem is solved with a first guess for the limits. The first guess, as in the short-term scenario, is for the IPoC limits to be proportional to the mixand weights (using the approximated version of Eq. (14b))

$$\bar{P}_{IC,cs} = \frac{\gamma_c}{n_{conj}} \bar{P}_{TIC} \quad c \in \{1, \dots, n_{mix}\} \quad s \in \{1, \dots, n_{conj}\}. \quad (53)$$

Only the optimization node where the TIPoC is maximum is used in the NLP because the maximum point in the profile is expected to stay the same or be shifted by a short time. This single value of TIPoC is indicated as $\hat{P}_{TIC} = \max_i(P_{TIC_i})$, where $i \in [0, N]$ and the correspondent values of IPoC for the single secondaries are \hat{P}_{IC_s} .

$$\min_{\rho, \alpha} |\rho| \quad (54a)$$

$$\text{s.t. } \mathbf{r} = \mathbf{r}^{ball} + \rho \hat{\mathbf{f}}, \quad (54b)$$

$$\bar{P}_{IC,cs} = \bar{P}_{TIC} \cdot 10^{-\alpha_{cs}} \quad c \in \{1, \dots, n_{mix}\} \quad s \in \{1, \dots, n_{conj}\}, \quad (54c)$$

$$\gamma_c \hat{P}_{IC,cs}(\Delta \mathbf{r}_{cs}, \mathbf{P}_{cs}, HBR_s) \leq \bar{P}_{IC,cs} \quad c \in \{1, \dots, n_{mix}\} \quad s \in \{1, \dots, n_{conj}\}, \quad (54d)$$

$$1 - \bar{P}_{TIC} - \prod_{s=1}^{n_{conj}} \prod_{c=1}^{n_{mix}} (1 - \bar{P}_{IC,cs}) = 0, \quad (54e)$$

$$0 \leq \rho \leq \rho^0, \quad (54f)$$

$$0 \leq \alpha_{cs} \leq 10 \quad c \in \{1, \dots, n_{mix}\} \quad s \in \{1, \dots, n_{conj}\}, \quad (54g)$$

where the position variables \mathbf{r} , \mathbf{r}^{ball} , $\Delta \mathbf{r}_{cs} \in \mathbb{R}^3$ are all computed at the time step of maximum TIPoC. In this case, the objective function in Eq. (54a) is the minimization of the scalar variable ρ . The remaining equations from Eq. (54b) to Eq. (54g) can be interpreted in the same way as those in Problem 41. The same considerations from Section III.C are also valid for the long-term encounters when propagating with a GMM.

E. Final Form of the Problem

This section summarizes the problem we face and provides some insights into the optimization process. First, we finalize the low-level optimization problem, the SOCP. The complete objective function is given by the sum of Eq. (23) and Eq. (27b):

$$J = \kappa_{vc} \sum_{i=0}^N v_i + \sum_{i=0}^{N-1} u_i \cdot \Delta t_i, \quad (55)$$

where the node-wise control action is weighted to account for variable time steps. The final SOCP is reported in Problem (56).

$$\min_{\mathbf{x}, \mathbf{u}} \text{Eq. (55)} \quad (56)$$

$$\text{s.t. Eq. (17), Eq. (29) or Eq. (32) with Eq. (36), Eqs. (21), (22), (24), (25) and (27a)}$$

The major iterations' convergence criterion is computed as the difference between the maximum control acceleration of two consecutive iterations

$$e_M = \max_i (||\mathbf{u}_i^j - \mathbf{u}_i^{j-1}||). \quad (57)$$

Likewise, the minor iterations' criterion (for the linearized SMD method) is the difference between the relative position

vectors of two consecutive minor iterations

$$e_m = \max_i (\|r_i^j - r_i^{j-1}\|). \quad (58)$$

It is relevant to remember that the successive linearization process is performed on the output of the previous optimization problem, so there is no online check on the accuracy of the forward-propagated solution. Such a check is performed after the optimization has reached convergence in all its levels. A validation error is computed as the maximum difference between the states at the last output of the optimization and the states obtained by forward-propagating the trajectory using the converged control profile

$$e_{validation} = \max_i (\|x_i^{j=end} - x_i^{val}\|). \quad (59)$$

To conclude the discussion, the high-level work-flow of the algorithm, as it has been presented in the previous sections, is shown in Fig. 1.

IV. Results

Realistic test cases for multiple encounters in LEO are analyzed. Three scenarios are considered. In the first one, the primary must deal with multiple short-term conjunctions with different secondaries; in the second one, the primary encounters the secondary more than once, and the uncertainties are propagated using GMM; in the last one, a long term encounter with a single secondary is studied using GMMs. Results from both the refinement methods from Section III.B and Section III.D are compared. In all the scenarios, the discretization time step is such that the orbit of the primary is divided into 60 nodes. The threshold TPoC and TIPoC are both set to 10^{-6} . The tolerance on the major iterations is set to 10^{-3} , and the one on the minor iterations for the linearized SMD method is set to 10^{-6} . The simulations are run with MATLAB r2022b on AMD Ryzen 9 6900HS @ 3.3GHz. The optimization is performed using MOSEK 10.0.24, which implements a state-of-the-art primal-dual interior-point solver. Scaled variables are used both during the integration of the equations of motion and in the optimization to favor numerical stability and convergence: the scaling constants are $L_{sc} = a_p$, $V_{sc} = \sqrt{\mu_E/a_p}$, $T_{sc} = \sqrt{a_p^3/\mu_E}$, and $A_{sc} = \mu_E/a_p^2$, where a_p and μ_E are the semi-major axis of the primary's orbit and Earth's gravitational constant. In all the considered scenarios, the trajectories are discretized using a constant time step into 60 nodes per orbit.

A. Case 1: Multiple Short-Term Encounters in LEO

Most impacts in LEO are head-to-head [1], so they involve very high relative velocities. The test case presented simulates a series of endogenous conjunctions in the Starlink constellation under $J2$ dynamics. A total of ten conjunctions happening in the course of ten orbits of the primary is synthetically generated. The primary is on a circular orbit with

an inclination of 53 deg, a radius of 6928 km, a RAAN, and an argument of periapsis equal to 0 deg; at the starting time, t_0 , its true anomaly is 0 deg. The parameters that define each conjunction are reported in Table 1 and Table 2: the relative states are expressed in the ECI reference frame, whereas the covariances are in the radial, along-track, cross-track (RTN) of the secondary. The covariance of the primary is assumed to be already absorbed by that of the secondary, so the number of parameters needed to set the scenario is reduced. $d_{miss} = \|\Delta \mathbf{r}_{s,CA}\|$ is the miss distance of the un-maneuvered case, and $\gamma_v = \text{acos}(\mathbf{v}_{p,CA} \cdot \mathbf{v}_{s,CA})$ is the angle between the velocity vectors of the two spacecraft; since the encounters happen between satellites on circular orbits at the same altitude, the magnitude of the velocity of the two spacecraft is equal. The HBR is the same for each Starlink satellite and is conservatively assumed to be 3 m. The propagation is performed using the harmonics up to the second degree of the gravitational field. The spacecraft is supposed to mount a low-thruster with a maximum thrust of 5.2 mN, which, considering the Starlink's mass of 230 kg, corresponds to a maximum acceleration of 0.02 mm/s². The algorithm is run with both the refinements methods

Table 1 Case 1: conjunctions' parameters.

	t_{CA}	$\Delta \mathbf{r}$ [m]	$\Delta \mathbf{v}$ [km/s]	d_{miss} [m]	P_C [-]	γ_v [deg]
CDM 1	1 h 34 min 3 s	[-11.45; -19.44 7.44]	[0.37; -2.85; 4.32]	23.8	0.0017	40
CDM 2	2 h 4 min 20 s	[99.90; 14.60 2.78]	[-3.94; -5.85; 3.36]	101.0	0.0018	62
CDM 3	3 h 43 min 11 s	[45.70; -3.73 28.29]	[-0.15; -1.30; 0.90]	53.9	0.0017	12
CDM 4	4 h 46 min 55 s	[8.90 49.27 -50.88]	[0.93; -0.63; 11.56]	71.4	0.0025	100
CDM 5	5 h 53 min 54 s	[-8.10 -3.02 -20.62]	[13.86; -3.71; -4.92]	22.4	0.0138	180
CDM 6	9 h 22 min 43 s	[-12.64 -14.81 13.76]	[5.64; -3.00 8.62]	23.8	0.0023	90
CDM 7	11 h 47 min 47 s	[2.09 13.74 1.89]	[7.93; -7.06; 3.21]	14.0	0.0022	94
CDM 8	13 h 17 min 3 s	[-4.18 -14.19 14.49]	[0.37; -2.23; 1.35]	20.7	0.0020	20
CDM 9	14 h 46 min 20 s	[8.92 -1.02 -12.78]	[1.43; 4.52; 13.58]	15.6	0.0050	143
CDM 10	15 h 56 min 28 s	[-19.88 9.10 -4.18]	[0.63; -9.52; -0.31]	22.3	0.0012	78

Table 2 Case 1: elements of the relative position covariance matrix of each conjunction.

	P_{rr} [km ²]	P_{tt} [km ²]	P_{nn} [km ²]	P_{rt} [km ²]	P_{tn} [km ²]	P_{nr} [km ²]
CDM 1	0.0078	0.2887	0.0145	0.0466	0.0103	0.0644
CDM 2	0.0662	0.1279	0.1170	-0.0918	0.0879	-0.1220
CDM 3	0.2473	0.0022	0.0616	0.0215	0.1232	0.0109
CDM 4	0.0004	0.1457	0.1649	-0.0055	0.0057	-0.1548
CDM 5	0.2579	0.0199	0.0333	-0.0710	-0.0924	0.0256
CDM 6	0.0001	0.2000	0.1110	-0.0007	0.0005	-0.1486
CDM 7	0.0015	0.2027	0.1069	-0.0162	0.0120	-0.1469
CDM 8	0.1814	0.0012	0.1284	-0.0142	-0.1523	0.0119
CDM 9	0.0028	0.0002	0.3081	-0.0003	0.0278	-0.0017
CDM 10	0.0004	0.1327	0.1779	-0.0036	0.0040	-0.1535

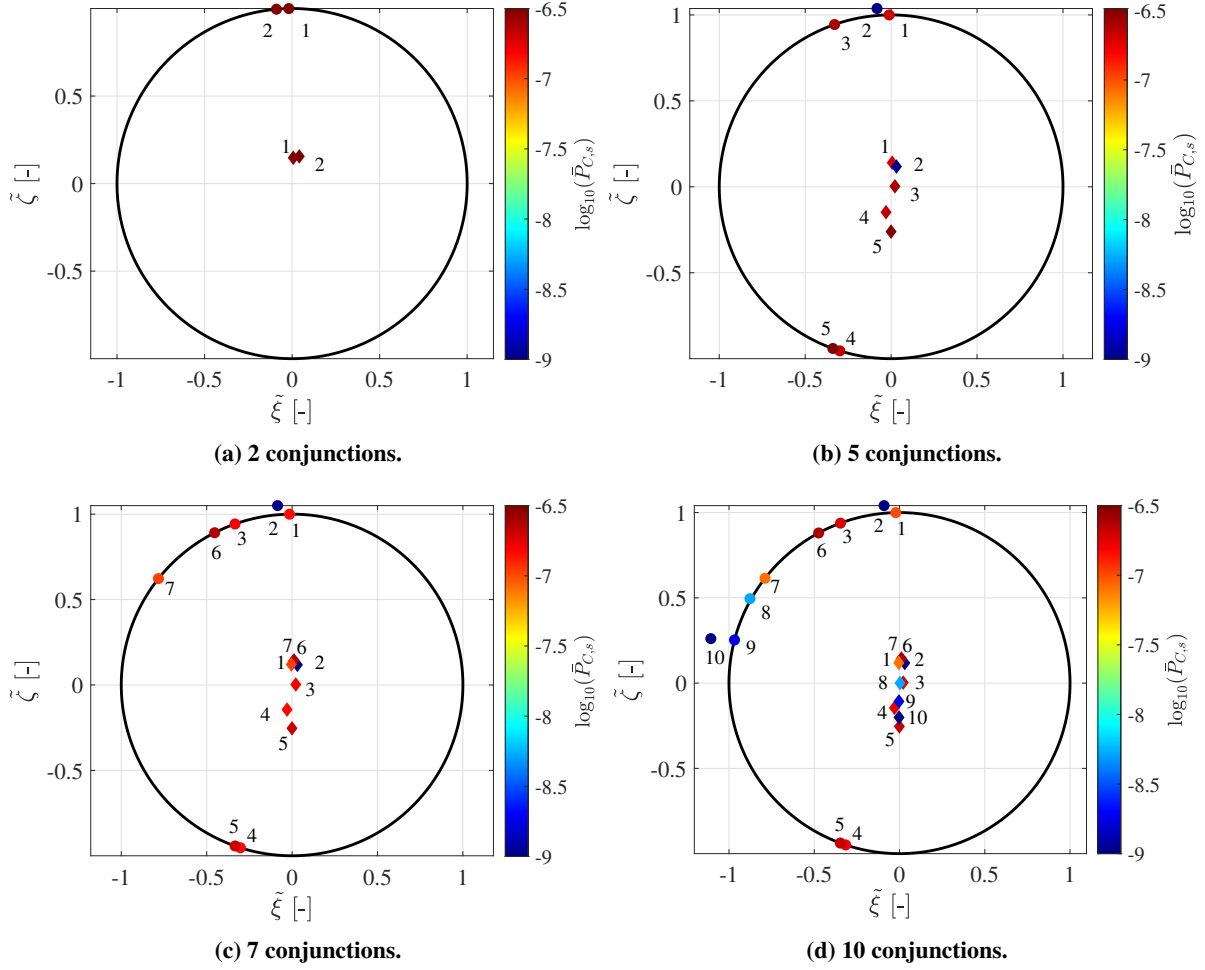


Figure 5 Case 1: equivalent B-plane representation of the conjunctions.

introduced in Section III.B, and the results are compared.

In Fig. 5, the equivalent B-planes of the conjunctions for each case considered are shown. To represent all the conjunctions in the same plot, a coordinate transformation is performed on the KOZ ellipse and on the relative position points. The transformation comprises a rotation to diagonalize the covariance matrix and a stretch to circularize it. Considering a generic vector $\mathbf{w} = [\xi \ \zeta]^T$ expressed in the B-plane reference frame of a conjunction s , the transformed vector $\tilde{\mathbf{w}} = [\tilde{\xi} \ \tilde{\zeta}]^T$ is

$$\tilde{\mathbf{w}} = \text{diag}([1/a; 1/b]) \mathbf{V} \mathbf{w}, \quad (60)$$

where $a, b \in \mathbb{R}_+$ are the semiaxes of the ellipse associated with the optimized probability threshold, and $\mathbf{V} \in \mathbb{R}^{2 \times 2}$ is the rotation matrix that diagonalizes the covariance. The ballistic trajectory points are shown as diamonds, and the optimized points obtained using the linearized SMD constraint with limit adaptation are shown as circles. The conjunction number is indicated for each marker, and the color of the marker is associated with the value of the limit

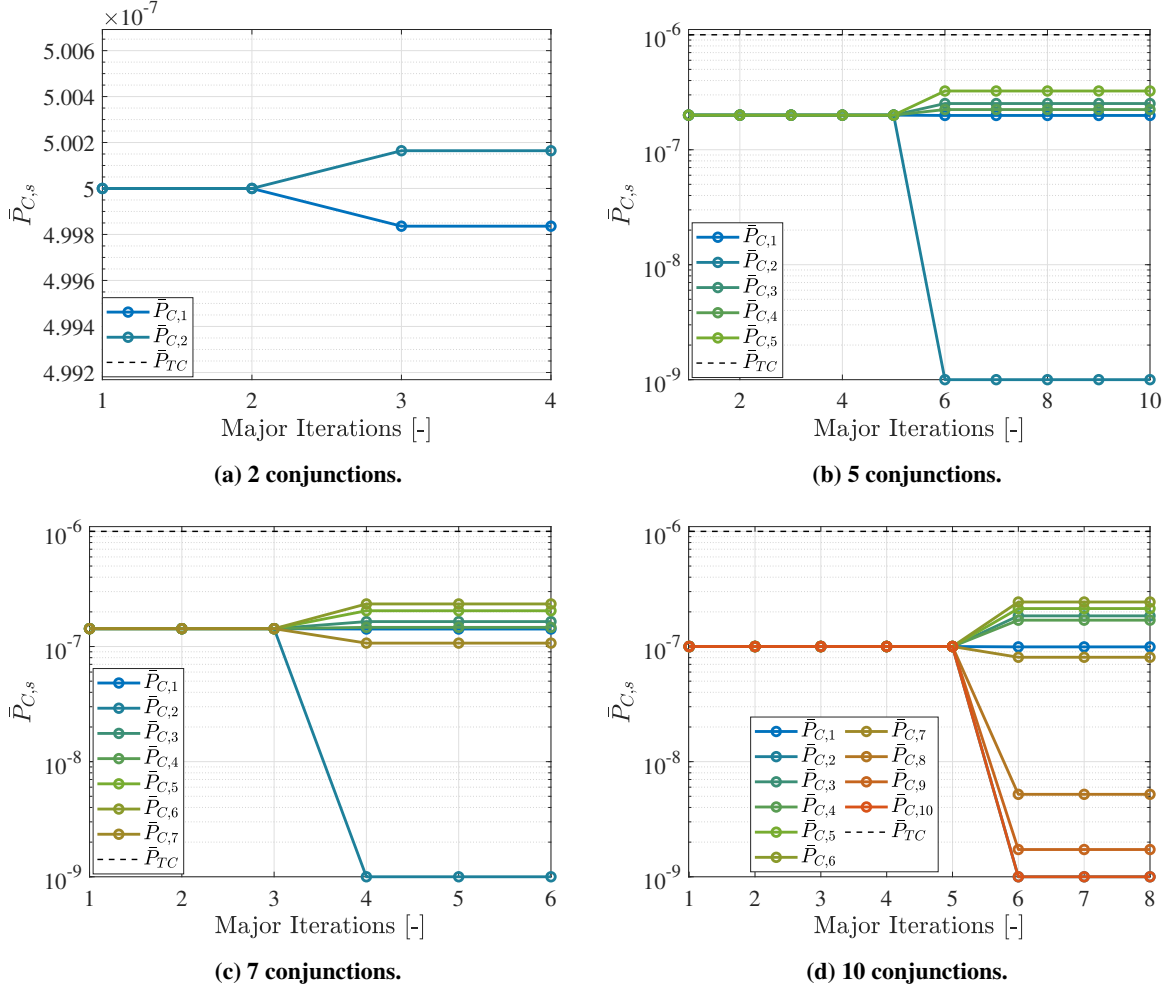


Figure 6 Case 1: evolution of the $\bar{P}_{C,s}$ of the single conjunctions.

PoC of the corresponding conjunction after the limit adaptation. The result of the same limit adaptation is reported in Fig. 6: after the first SCP is solved, in all the considered cases, a single SCP is needed to find a solution that grants a TPoC value sufficiently close to the threshold. We notice from Fig. 6 that depending on the conjunctions configuration and their number, the algorithm automatically finds the most important ones and assigns them a higher weight. For example, the second conjunction is equally important to the first one in the first scenario, but it becomes irrelevant in the next ones. As a second example, the last three conjunctions that differentiate the last scenario from the third have no effect on the final result since their \bar{P}_C value drops significantly after the adaptation. This is why the computed maneuvers for the last two scenarios are almost identical (see Fig. 7c and Fig. 7d).

Through an analysis of this type, it is also possible to identify clusters of conjunctions that cause a maneuver. Indeed, the time, direction, and magnitude of the first two burns remain almost unchanged across the four cases. In general, the maneuvers are all mainly in the tangential direction. This confirms the idea proposed by other researchers [2, 4] that raising or lowering the orbit is the most effective way of performing the CAM if enough warning time is given.

Table 3 Case 1: compared results for the SMD and TPoC linearized constraints.

Constraint	Linearized SMD				Linearized TPoC				
	n_{conj}	2	5	7	10	2	5	7	10
Δv [mm/s]		21.16	60.05	102.04	102.14	21.16	62.32	103.18	105.58
$P_{TC} \times 10^6$ [-]		1.001	1.001	1.001	0.998	1.002	0.801	0.824	0.583
n_{major} [-]		4	6	6	8	5	7	10	20
n_{minor} [-]		5	9	10	13	-	-	-	-
$e_{validation}$ [mm]		0.92	1.88	0.72	5.12	37.61	5.48	43.40	1940.80
T_{sim} [s]		4.53	8.34	14.52	28.03	4.47	8.82	20.66	62.15

In Table 3, the results in terms of final TPoC and Δv are shown for the four combinations of conjunctions considered. Convergence results are also compared in the number of iterations, convergence time, and maximum positional validation error. The two refinement methods do not differ greatly in the resulting Δv profile or in the final equivalent B-plane configuration, as is shown in Table 3. Nonetheless, the method that relies on the linearized SMD constraint with limit adaptation yields more accurate results and can target the desired TPoC threshold with higher precision. The PoC value at TCA for the first method is always kept below the threshold value with a margin of .002%, while the linearized TPoC method reaches TPoC values up to 42% below the threshold. This means that the CAM optimization does not find the optimal result with the second method, leading to higher Δv impulses than the first method. The run times of the two methods are similar when a low number of conjunctions is considered, but the linearized SMD method is definitely faster when we start to consider a high n_{conj} . In general, we can infer that the linearized SMD constraint is more appropriate when dealing with more than two conjunctions because each PoC constraint is linearized separately, so the coarseness of approximation of the nonlinearity does not scale with the complexity of the problem.

B. Case 2: Repeating Short-Term Encounter in LEO with GMM

Let us consider a scenario in which a secondary spacecraft's orbit intersects the primary's twice, thus generating a repeating encounter. The first encounter is described by a CDM, whereas the second one is detected by propagating the dynamics. The covariance of the secondary at the first TCA is split into a number of GMM mixands, which are propagated separately until the second TCA. Here, we assume that the covariance of the primary is negligible w.r.t. to the secondary's. The state of the primary is described at TCA by $a = 6800$ km, $e = 0$, $\omega = \Omega = \theta = 0$ deg, and $i = 91.67$ deg; the orbit of the secondary is elliptical, has opposite inclination w.r.t. the primary and its period is a multiple of the period of the primary. The full secondary's covariance matrix at the first TCA is defined in RTN coordinates in Table 4. The primary covariance matrix is assumed to be null.

According to reference [21], when propagating Cartesian coordinates in LEO, for typical initial uncertainty, after five orbits ca., the normality of the distribution is lost. So, we construct the test such that after six orbits of the primary,

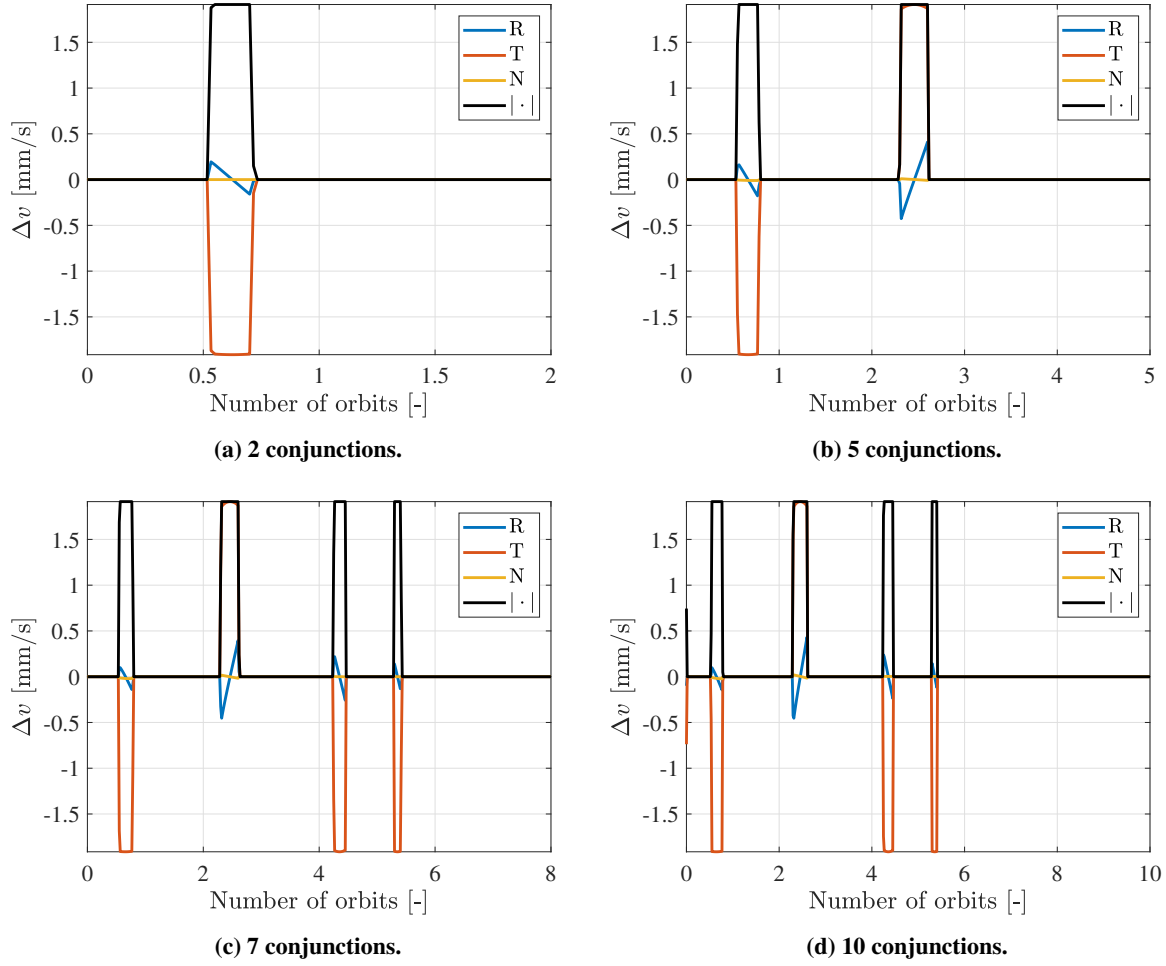


Figure 7 Case 1: Δv to perform the CAM.

Table 4 Case 2: elements of the relative position covariance matrix at the first TCA.

Spacecraft	P_{rr} [m ²]	P_{tt} [m ²]	P_{nn} [m ²]	$P_{\dot{r}\dot{r}}$ [mm ² /s ²]	$P_{\dot{t}\dot{t}}$ [mm ² /s ²]	$P_{\dot{n}\dot{n}}$ [mm ² /s ²]
Primary	0	0	0	0	0	0
Secondary	2.025	10.000	2.500	0.225	5.625	0.625

the head-to-head encounter happens again. The eccentricity of the secondary orbit is 0.6971; its semi-major axis is 22453.1 km, the inclination is 181.67 deg, the argument of perigee is 0 deg, the RAAN is $1.72 \cdot 10^{-3}$ deg and the true anomaly at the first conjunction is 0.11 deg. The orbits are propagated backward for one orbital period of the primary and forward up to the second conjunction. In this way, the first conjunction is treated as a standard one, i.e., without splitting, and the second one is treated with the propagated GMM components. In this case, we are considering a chemical propulsion system with a maximum instantaneous acceleration of 1 mm/s². Different simulations with different n_{mix} are compared to one where no split is performed, i.e., the second conjunction is treated with a linearly

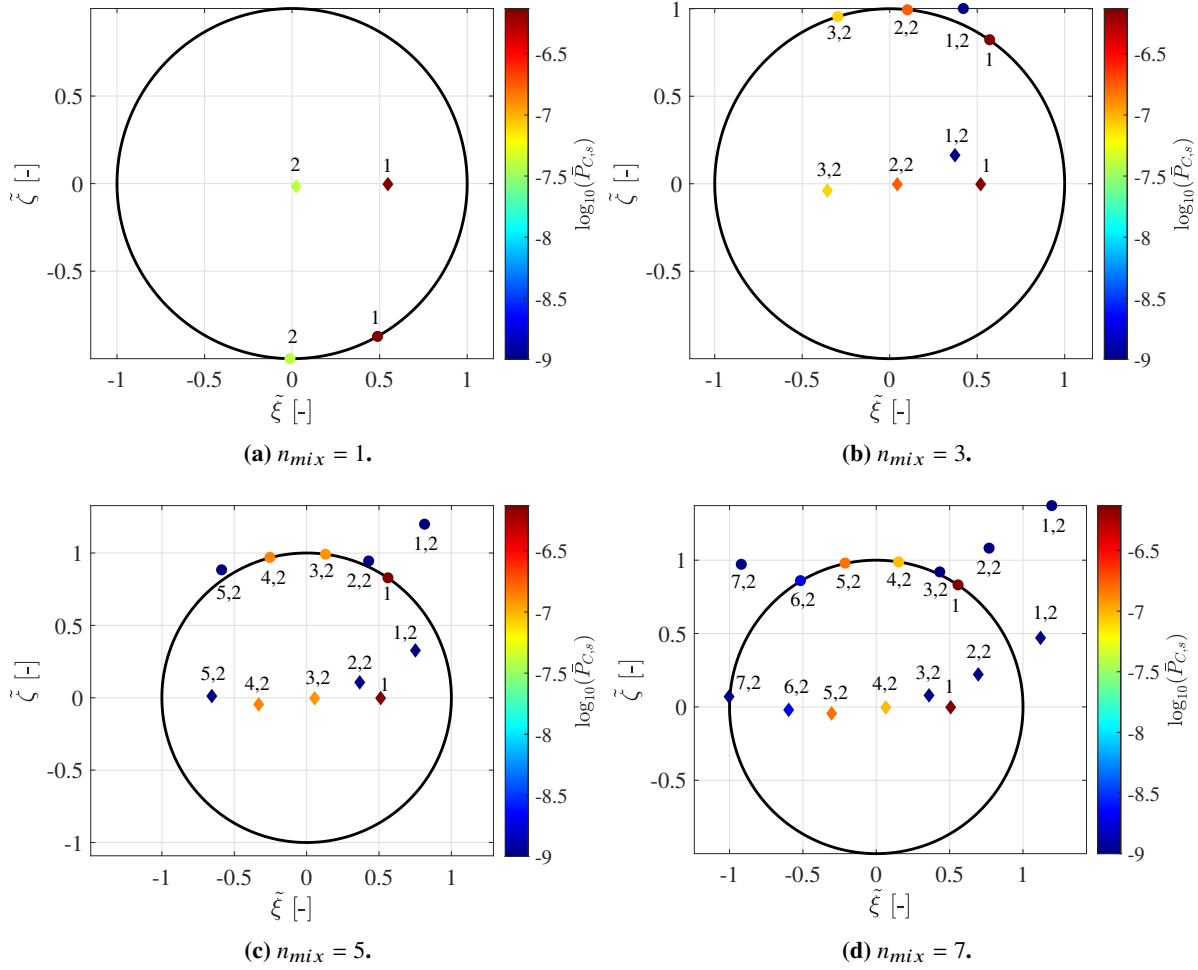


Figure 8 Case 2: equivalent B-plane representation of the conjunctions.

propagated covariance. Moreover, the solutions obtained with the two constraints are compared in Table 5.

In Table 5, we notice that the use of the GMM permits better to represent the KOZ and reduce the required Δv by at least 4 mm/s. Fig. 8 shows the equivalent B-planes of the two conjunctions for different values of n_{mix} . The first conjunction is always dominant: since it appears first avoiding it means that the satellite will most likely avoid the subsequent one as well. Nonetheless, in the other plots, it is useful to see which mixands play a role in defining the limits: in particular, in Fig. 8b mixands 3 and 2, in Fig. 8c mixands 4 and 3 and in Fig. 8d mixands 5 and 4 are the ones that are not led to the lowest threshold. This means that in the second (extended) conjunction, the primary passes closest to the central mixand and the one right after it compared to all the others. For all the other mixands, the threshold PoC is brought down to the minimum value of 10^{-9} , meaning they do not play a role in defining the maneuver.

Depending on the number of mixands used, the TCAs of the single mixands are between 1.32 and 2.91 s apart from each other, which is accounted for in the selection of the time grid for the discretization. This happens because the encounter is head-to-head, and the split is performed very close to the direction of the velocity of the secondary so

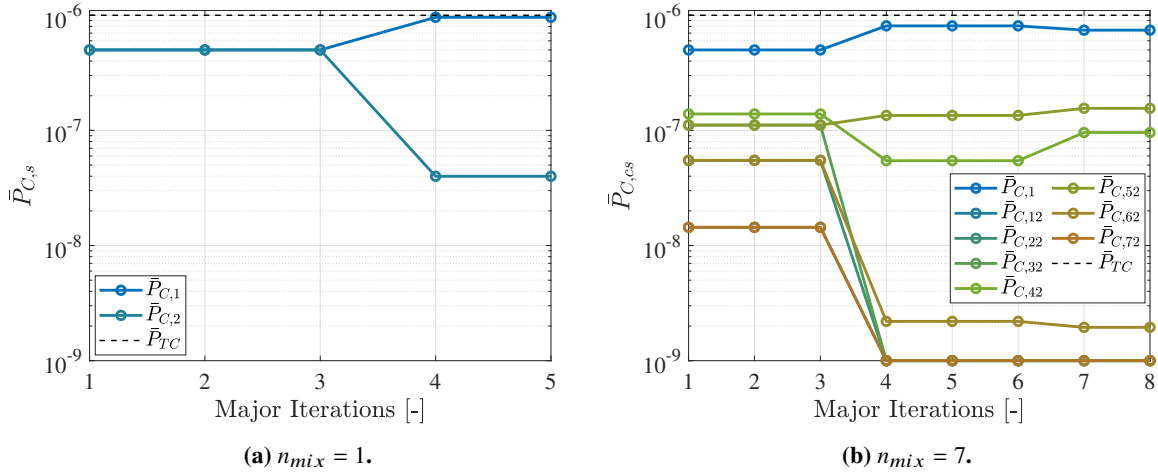


Figure 9 Case 2: evolution of the $\bar{P}_{C,s}$ of the single conjunctions and mixands.

that the primary runs into each mixand consecutively, as Fig. 3a illustrates. In Fig. 9, the adaptation of the limits for two representative numbers of mixand is shown: with no GMM split, the first conjunction dominates the final TPoC computation, while in the case with $n_{mix} = 7$, the second conjunction is considered slightly more important. In Table 6, one sees that, in accordance with most published research on single encounters [4], in all the considered cases, the Δv is almost purely tangential. Nonetheless, in the case where no split is performed, the direction of thrust is opposite to that of the other cases. In Fig. 8a, the reader can see that the tangential maneuver moves the relative position along the $\tilde{\xi}$ axis, so there is little to no difference in performing a maneuver on the positive or the negative tangential direction and the optimizer prefers one over the other. In all cases with a split, the preferred maneuver is in the positive tangential direction. The number of mixands considered does not affect the maneuvering time. The maneuver is always performed half an orbit before the first TCA, and an almost negligible second maneuver is performed half an orbit before the second TCA.

Regarding the convergence properties, the two methods behave similarly to the case in Section IV.A, with the first method being slightly faster when more mixands are considered. In this case, though, it is important to point out that because of the coarseness of the linearization, the linearized TPoC method always reaches a solution that is around 5% over the TPoC threshold. This allows it to find a lower Δv at the cost of precision. The validation error for both methods is always acceptable.

C. Case 3: Single Long-Term Encounter in LEO with GMM

In this scenario, a single long-term conjunction in LEO is studied with GMM. The problem becomes equivalent to having a long-term conjunction with multiple secondaries. The scenario is taken from the LEO test case of reference [19]: the primary spacecraft is on a circular LEO with $a = 6800$ km, and $\omega = \Omega = i = \theta = 0$ deg; the relative state of

Table 5 Case 2: compared results for the SMD and TPoC linearized constraints.

Constraint	Linearized SMD				Linearized TPoC			
	1	3	5	7	1	3	5	7
n_{mix}	1	3	5	7	1	3	5	7
Δv [mm/s]	57.06	52.64	52.98	53.37	56.52	52.23	52.55	52.15
$P_{TC} \times 10^6$ [-]	1.002	0.968	0.936	0.910	1.053	1.039	1.038	1.048
n_{major} [-]	5	8	8	8	7	7	8	9
n_{minor} [-]	12	16	16	19	-	-	-	-
$e_{validation}$ [mm]	9.92	3.64	3.21	2.98	0.46	3.81	4.81	10.61
T_{sim} [s]	6.57	19.76	23.01	27.68	9.15	16.98	24.58	30.17

Table 6 Case 2: Δv to perform the CAM.

n_{mix}	t_1 [s]	R_1 [mm/s]	T_1 [mm/s]	N_1 [mm/s]	t_2 [s]	R_2 [mm/s]	T_2 [mm/s]	N_2 [mm/s]
1	2790.26	-0.69	-56.63	-0.04	25112.31	0	-0.04	0
3	2790.26	-0.68	52.60	0.01	25112.31	0	0.03	0
5	2790.26	-0.67	53.04	0.01	25112.31	0 0.08		0
7	2790.26	-0.01	53.37	0.25	-	-	-	-

Table 7 Case 3: elements of the relative position covariance matrix of the two spacecraft.

Spacecraft	C_{rr} [m ²]	C_{tt} [m ²]	C_{nn} [m ²]	$C_{\dot{r}\dot{r}}$ [m ² /s ²]	$C_{\dot{t}\dot{t}}$ [m ² /s ²]	$C_{\dot{n}\dot{n}}$ [m ² /s ²]
Primary	0.625	10	3.025	0.00625	0.05625	0.00225
Secondary	5.625	90	27.225	0.05625	0.50625	0.02025

the secondary as expressed in the primary's RTN at TCA, i.e., at the starting time is

$$\mathbf{x}_{rel} = [-1.004814 \ 0 \ 0 \ 0.112790 \ 3.388089 \ 0.011228]^T,$$

where the first three elements are in [km] and the last three in [m/s]. The covariance matrices of the two spacecraft are reported in Table 7. The combined HBR is 32 m, and the maximum instantaneous acceleration achievable by the primary is 0.2 mm/s², corresponding to a maximum thrust of 40 mN in a 200 kg satellite. The dynamics include J2 perturbation, lunisolar attraction, atmospheric drag, and solar radiation pressure (SRP). The models used to compute the perturbation forces are computed with Accurate Integrator for Debris Analysis (AIDA) [50]. The physical parameters of the spacecraft are reported in Table 8.

The propagation spans six orbits of the primary from TCA. Different orders of the GMM are compared in terms of Δv , TPoC profile, and convergence properties in Table 9 and Fig. 10. It is interesting to notice from Fig. 10a that, when a low n_{mix} is used, after four orbits, the profile tends to lose its periodicity property, which is instead preserved for a high n_{mix} . This suggests that the 3D KOZ starts to become too wide when no GMM is used, while it is represented

more accurately when n_{mix} is high enough. In Fig. 11, the contribution of each mixand to the ballistic TIPoC is shown for three (Fig. 11a) and seven (Fig. 11b) mixands. It is clear that having more mixands allows us to refine where the majority of the probability resides. In Fig. 11a, the total probability is mostly given by the first mixand. Instead, in Fig. 11b, we see that most of the mixands do not contribute at all, being below 10^{-9} , and the highest contributions are given by mixands 2, 3, and 1. Moreover, using seven mixands allows us to preserve the profile's periodicity, which starts to fade when three mixands are used because $P_{IC,3}$ has a non-negligible effect given by the inflation of the corresponding covariance.

In Fig. 12, the Δv profiles for the four considered cases are reported. The computed maneuver is very similar, and the normal component is always predominant. From Table 9, we see that the linearized SMD approach is much more efficient in this test case: the solution requires fewer major iterations, and the Δv is always lower. Since there is no guarantee for either method to find the global optimum, we observe that the solution found in the two cases falls into two different local minimum wells. In fact, the TIPoC profile in the case with $n_{mix} = 1$ had three equivalent points of global maxima. The linearized SMD method's solution for any n_{mix} preserves the second maximum (around 1.3 orbital periods), while the linearized TIPoC one preserves the first maximum (around 0.73 orbital periods). The solution found by the first method is closer to the global optimum. Moreover, most importantly, the second method with $n_{mix} = 7$ finds a solution that is far from the local optimum achieved by $n_{mix} = 3$ and $n_{mix} = 5$, so the linearization starts to be too coarse when more than five mixands are considered in this test case.

Table 8 LEO scenario: physical properties of the spacecraft.

Spacecraft	m [kg]	A_{drag} [m ²]	C_D [-]	A_{SRP} [m ²]	C_r [-]	HBR [m]
Primary	200	1	2.2	1	1.31	25
Secondary	50	0.05	2	0.05	1.31	7

Table 9 Case 3: compared results for the SMD and TIPoC linearized constraints.

Constraint	Linearized SMD				Linearized TIPoC		
	1	3	5	7	3	5	7
n_{mix} [-]	1	3	5	7	3	5	7
Δv [mm/s]	339.42	342.30	344.12	367.77	401.76	420.78	469.08
$\max_i(P_{TIC,i}) \times 10^{-6}$ [-]	1.006	9.93	0.989	0.829	1.000	1.000	0.196
n_{major} [-]	4	9	6	7	7	7	20
n_{minor} [-]	15	21	30	15	-	-	-
$e_{validation}$ [mm]	12.73	47.06	1.63	30.79	53.43	44.39	20.32
T_{sim} [s]	52.85	134.75	164.58	142.02	100.63	114.00	272.64

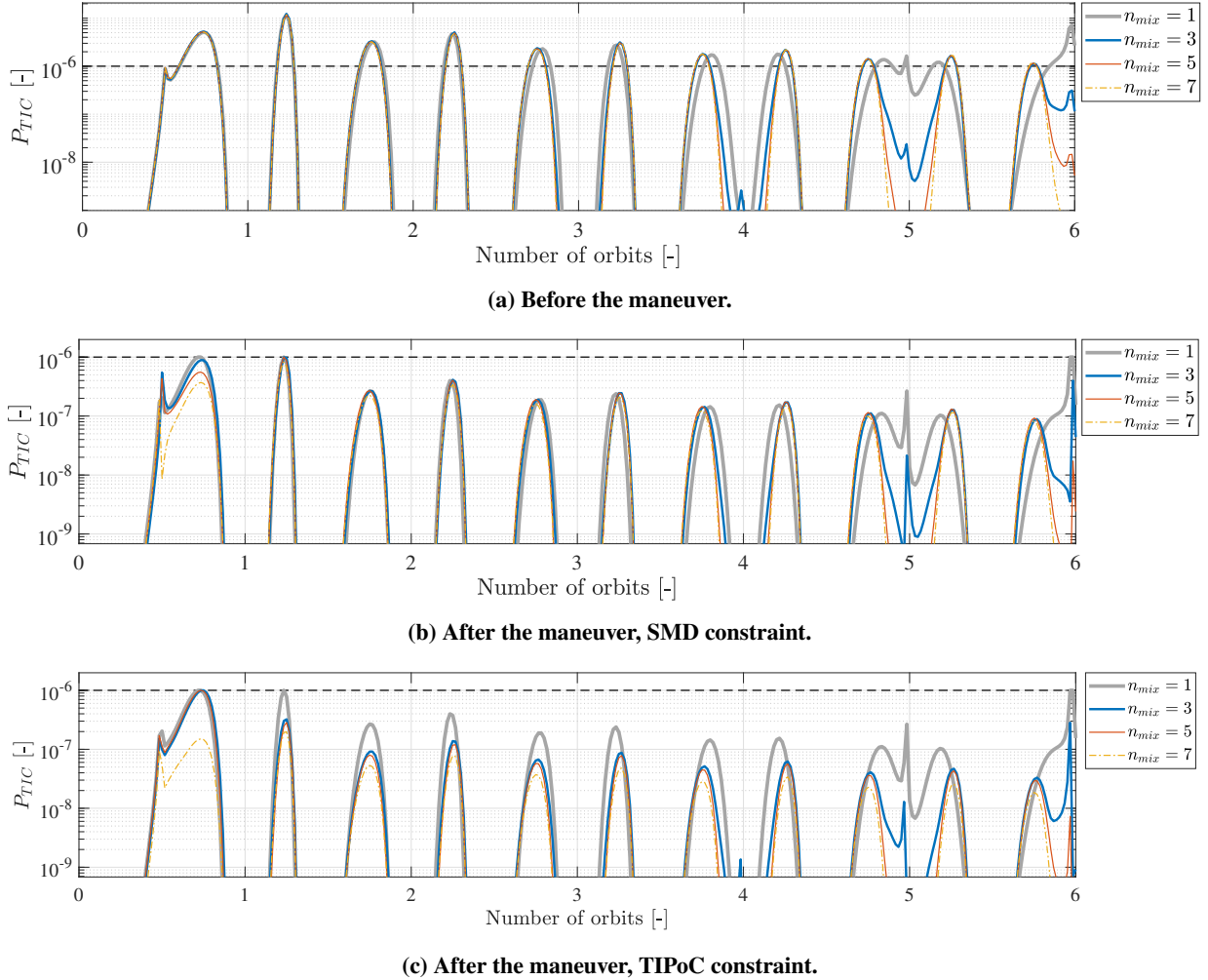
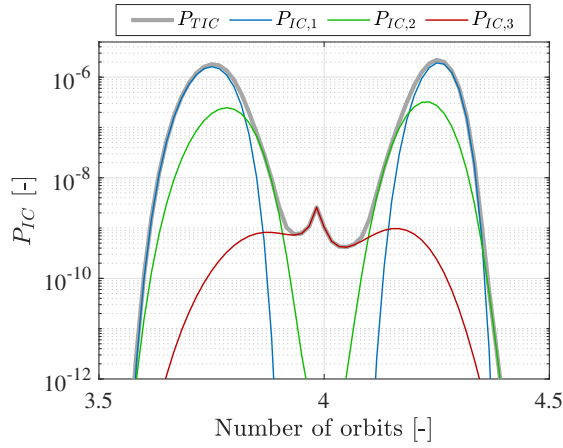


Figure 10 Case 3: TIPoC profile for different n_{mix} in the long-term encounter scenario.

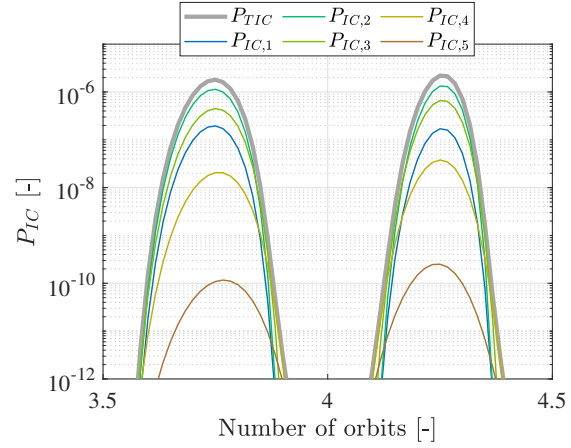
V. Conclusions

This work presented a sequential convex program (SCP) method to compute collision avoidance maneuvers (CAMs) in scenarios involving multiple encounters between satellites. Both short-term and long-term encounters were considered. In the first case, the total probability of collision (TPoC) was used as a collision metric, whereas in the second, we used the total instantaneous probability of collision (TIPoC). Moreover, for the scenarios in which uncertainty propagation is needed for long periods, we employed a Gaussian mixture model (GMM) method to propagate the uncertainty of the secondary spacecraft and define multiple keep-out zones.

The fuel-optimal CAM optimization problem was cast as a second-order cone program (SOCP), where different techniques were used to convexify the non-convex constraints. Two methods were proposed to refine the initial SCP solution. The first one relies on a DA-based linearization of the TPoC or TIPoC constraint; the second one updates the probability of collision (PoC) or instantaneous probability of collision limits associated with the single conjunctions by

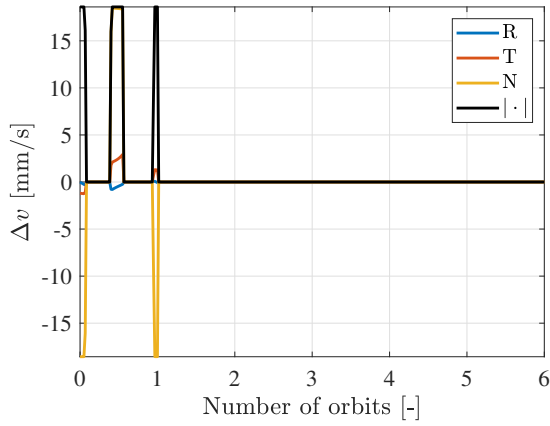


(a) $n_{mix} = 3$.

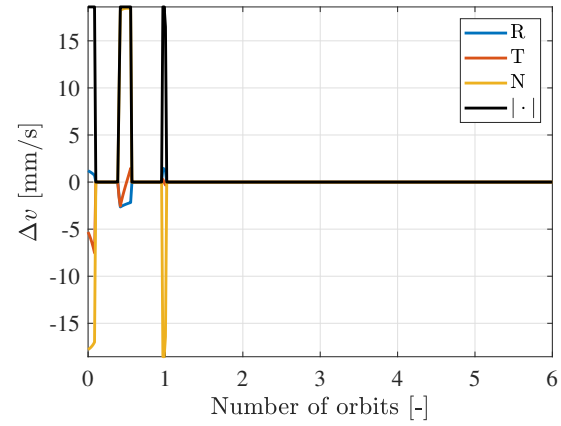


(b) $n_{mix} = 7$: the contribution of mixands 6 and 7 is negligible.

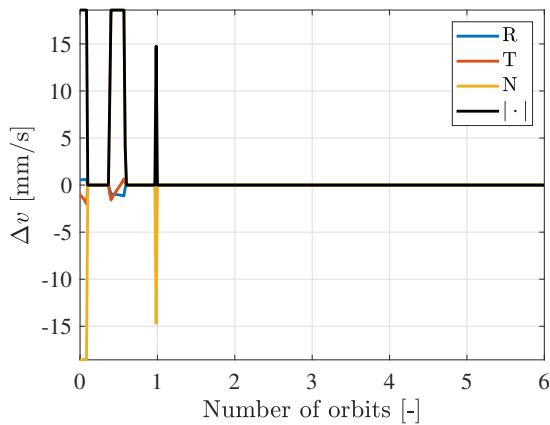
Figure 11 Case 3: Breakdown of the contribution of each mixand to the TIPoC. Zoom in a central orbit.



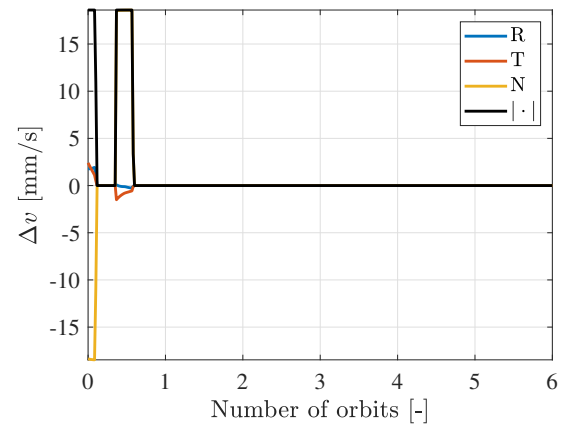
(a) $n_{mix} = 1$.



(b) $n_{mix} = 3$.



(c) $n_{mix} = 5$.



(d) $n_{mix} = 7$.

Figure 12 Case 3: Δv to perform the CAM.

means of a non-linear program.

The proposed methods were tested on three scenarios. The first one comprised multiple consecutive short-term conjunctions: Chan's PoC method was used to assess the risk, and the results for the two refinements algorithms were compared. The second scenario was a double encounter with the same secondary where the covariance was propagated with a GMM. The last one was a single long-term encounter studied with the aid of GMMs with different numbers of mixands. The algorithms can always find an optimal solution for the fuel-optimal problem, but global optimality is not guaranteed. The SMD linearization refinement method was deemed more suitable because it behaved much better in the presence of significant non-linearities of the original problem.

The proposed method is general, being able to deal with very diverse settings, including (i) both short- and long-term encounters, (ii) arbitrary dynamics models, (iii) arbitrary number of encounters, (iv) nonlinear propagation of the uncertainty of the secondary. The primary's uncertainty is propagated linearly when necessary. Since we assume that accurate orbit determination is performed on the maneuverable satellite, the initial uncertainty of the primary is almost negligible with respect to the secondary. If the uncertainty of the primary is larger, a nonlinear propagation model must also be used for the uncertainty of the primary.

In an ever more cluttered orbital environment, we believe that the complexity of the CA scenarios for spacecraft will increase dramatically. Given its light computational burden and proven efficacy and reliability in dealing with multiple conjunctions, the proposed algorithm can be an enabling tool for the safe use of Earth's space in the future.

Funding Sources

This material is based upon work supported by the Air Force Office of Scientific Research under award number FA2386-21-1-4115.

References

- [1] ESOC, "ESA's Annual Space Environment Report," Tech. rep., ESA, 2023.
- [2] Bombardelli, C., and Hernando-Ayuso, J., "Optimal impulsive collision avoidance in low earth orbit," *Journal of Guidance, Control, and Dynamics*, Vol. 38, AIAA International, 2015, pp. 217–225. <https://doi.org/10.2514/1.G000742>.
- [3] Gonzalo, J. L., Colombo, C., and Di Lizia, P., "A semi-analytical approach to low-thrust collision avoidance manoeuvre design," *70th International Astronautical Congress (IAC)*, Vol. 70, 70th International Astronautical Congress, Washington D.C., 2019, pp. 21–25.
- [4] Hernando-Ayuso, J., and Bombardelli, C., "Low-thrust collision avoidance in circular orbits," *Journal of Guidance, Control, and Dynamics*, Vol. 44, No. 5, 2021, pp. 983–995. <https://doi.org/10.2514/1.G005547>.

- [5] Armellin, R., “Collision avoidance maneuver optimization with a multiple-impulse convex formulation,” *Acta Astronautica*, Vol. 186, 2021, pp. 347–362. <https://doi.org/10.1016/j.actaastro.2021.05.046>.
- [6] Kim, E. H., Kim, H. D., and Kim, H. J., “A Study on the collision avoidance maneuver optimization with multiple space debris,” *Journal of Astronomy and Space Sciences*, Vol. 29, No. 1, 2012, pp. 11–21. <https://doi.org/10.5140/JASS.2012.29.1.011>.
- [7] Lee, K., Park, H., Park, C., and Park, S. Y., “Sub-optimal cooperative collision avoidance maneuvers of multiple active spacecraft via discrete-time generating functions,” *Aerospace Science and Technology*, Vol. 93, 2019, p. 105298. <https://doi.org/10.1016/J.AST.2019.07.031>.
- [8] Frigm, R. C., Hejduk, M. D., Johnson, L. C. ., and Plakalovic, D., “Total Probability of Collision as a Metric for Finite Conjunction Assessment and Collision Risk Management,” *Advanced Maui Optical and Space Surveillance Technologies (AMOS) Conference*, Maui, Hawaii, 2015.
- [9] Sánchez, L., and Vasile, M., “Constrained Optimal Collision Avoidance Manoeuvre Allocation under Uncertainty for Subsequent Conjunction Events,” *72nd International Astronautical Congress, IAC*, Vol. A6, Dubai, United Arab Emirates, 2021.
- [10] Masson, M., Arzelier, D., Joldes, M., Revelin, B., and Thomassin, J., “Multi-maneuver algorithms for multi-risk collision avoidance via nonconvex quadratic optimization,” *IFAC-PapersOnLine*, Vol. 56, No. 2, 2023, pp. 1995–2000. <https://doi.org/10.1016/j.ifacol.2023.10.1094>, URL <https://linkinghub.elsevier.com/retrieve/pii/S2405896323014970>.
- [11] Patera, R., “Satellite Collision Probability for Non-Linear Relative Motion,” *AIAA/AAS Astrodynamics Specialist Conference and Exhibit*, Vol. 26, American Institute of Aeronautics and Astronautics, Reston, Virigina, 2002. <https://doi.org/10.2514/6.2002-4632>.
- [12] De Vittori, A., Dani, G., Di Lizia, P., and Armellin, R., “Numerically Efficient Low-Thrust Collision Avoidance Maneuver Design in GEO Regime with Equinoctial Orbital Elements,” *2nd ESA NEO and Debris Detection Conference*, January, ESA/ESOC, Darmstadt, Germany, 2023.
- [13] De Vittori, A., Dani, G., Di Lizia, P., and Armellin, R., “Low-Thrust Collision Avoidance Design for Leo Missions With Return To Nominal Orbit,” *33rd AAS/AIAA Space Flight Mechanics Meeting*, Austin, TX, 2023, pp. 1–18.
- [14] De Vittori, A., Omodei, M., Di Lizia, P., Armellin, R., Gago, P., Torras Ribell, M., Antón, J., and Antón, D., “Numerically Efficient Low-Thrust Fuel-Optimal Collision Avoidance Maneuvers With Tangential Firings,” *AAS/AIAA Astrodynamics Specialist Conference*, 2023.
- [15] Dutta, S., and Misra, A. K., “Convex optimization of collision avoidance maneuvers in the presence of uncertainty,” *Acta Astronautica*, Vol. 197, 2022, pp. 257–268. <https://doi.org/10.1016/j.actaastro.2022.05.038>.
- [16] Mueller, J., “Onboard Planning of Collision Avoidance Maneuvers Using Robust Optimization,” *AIAA Infotech@Aerospace Conference*, American Institute of Aeronautics and Astronautics, Reston, Virigina, 2009. <https://doi.org/10.2514/6.2009-2051>.

- [17] Serra, R., Arzelier, D., Joldes, M., and Rondepierre, A., “Probabilistic Collision Avoidance for Long-term Space Encounters via Risk Selection,” *Advances in Aerospace Guidance, Navigation and Control*, Springer International Publishing, 2015, pp. 679–698. https://doi.org/10.1007/978-3-319-17518-8_39.
- [18] Pavanello, Z., Pirovano, L., and Armellin, R., “Long-Term Encounters Collision Avoidance Maneuver Optimization with a Convex Formulation,” *33rd AAS/AIAA Space Flight Mechanics Meeting*, Austin, TX, 2023, pp. 1–20.
- [19] Pavanello, Z., Pirovano, L., and Armellin, R., “Fuel-Optimal Collision Avoidance Maneuvers in Long-Term Encounters with Station-Keeping Constraints,” , 2023. URL <http://arxiv.org/abs/2307.06004>.
- [20] Luo, Y.-z., and Yang, Z., “A review of uncertainty propagation in orbital mechanics,” *Progress in Aerospace Sciences*, Vol. 89, 2017, pp. 23–39. <https://doi.org/10.1016/j.paerosci.2016.12.002>.
- [21] Yanez, C., Gupta, M., Morand, V., and Dolado, J. C., “On the Gaussianity validity time for orbital uncertainty propagation,” *1st NEO and Debris Detection Conference*, Vol. 2019-October, 2019, pp. 22–24.
- [22] Vittaldev, V., “Uncertainty propagation and conjunction assessment for resident space objects,” Ph.D. thesis, The University of Texas at Austin, 2015.
- [23] Dutta, S., and Misra, A. K., “Comparison between convex and non-convex optimization methods for collision avoidance maneuvers by a spacecraft,” *Acta Astronautica*, Vol. 202, No. May 2022, 2023, pp. 900–908. <https://doi.org/10.1016/j.actaastro.2022.06.020>.
- [24] Malyuta, D., Yu, Y., Elango, P., and Açıkmeşe, B., “Advances in trajectory optimization for space vehicle control,” *Annual Reviews in Control*, Vol. 52, 2021, pp. 282–315. <https://doi.org/10.1016/j.arcontrol.2021.04.013>, URL <https://linkinghub.elsevier.com/retrieve/pii/S1367578821000377>.
- [25] Li, J. S., Yang, Z., and Luo, Y. Z., “A review of space-object collision probability computation methods,” *Astrodynamics*, Vol. 6, No. 2, 2022, pp. 95–120. <https://doi.org/10.1007/s42064-021-0125-x>.
- [26] Pirovano, L., and Armellin, R., “Detection and estimation of spacecraft maneuvers for catalog maintenance,” *Acta Astronautica*, Vol. 215, No. December 2023, 2024, pp. 387–397. <https://doi.org/10.1016/j.actaastro.2023.12.016>.
- [27] Boyd, S., and Vandenberghe, L., *Convex Optimization*, Cambridge University Press, Cambridge, NY, 2004.
- [28] Malyuta, D., Reynolds, T. P., Szmuk, M., Lew, T., Bonalli, R., Pavone, M., and Açıkmeşe, B., “Convex Optimization for Trajectory Generation: A Tutorial on Generating Dynamically Feasible Trajectories Reliably and Efficiently,” *IEEE Control Systems*, Vol. 42, No. 5, 2022, pp. 40–113. <https://doi.org/10.1109/MCS.2022.3187542>.
- [29] Losacco, M., Fossà, A., and Armellin, R., “Low-Order Automatic Domain Splitting Approach for Nonlinear Uncertainty Mapping,” *Journal of Guidance, Control, and Dynamics*, 2024, pp. 1–20. <https://doi.org/10.2514/1.G007271>.
- [30] Bernardini, N., Wijayatunga, M. C., Baresi, N., and Armellin, R., “State-Dependent Trust Region for Successive Convex Optimization of Spacecraft Trajectories,” *33rd AAS/AIAA Space Flight Mechanics Meeting*, Austin, TX, 2023, pp. 1–20.

- [31] Alfriend, K. T., Akella, M. R., Frisbee, J., Foster, J. L., Lee, D.-J., and Wilkins, M., “Probability of collision error analysis,” *Space Debris*, 1999. <https://doi.org/https://doi.org/10.1023/A:1010056509803>.
- [32] De Vittori, A., Palermo, M. F., Di Lizia, P., and Armellin, R., “Low-Thrust Collision Avoidance Maneuver Optimization,” *Journal of Guidance, Control, and Dynamics*, Vol. 45, No. 10, 2022, pp. 1815–1829. <https://doi.org/10.2514/1.G006630>.
- [33] Zhang, S., Fu, T., Chen, D., and Cao, H., “Satellite instantaneous collision probability computation using equivalent volume cuboids,” *Journal of Guidance, Control, and Dynamics*, Vol. 43, No. 9, 2020, pp. 1757–1763. <https://doi.org/10.2514/1.G004711>.
- [34] Chan, K., “International Space Station Collision Probability,” *The Aerospace Corporation, Chantilly, VA, USA*, Vol. 6, No. 2, 2009, pp. 307–314.
- [35] Alfano, S., “Review of conjunction probability methods for short-term encounters,” *Advances in the Astronautical Sciences*, 2007.
- [36] Coppola, V. T., “Including velocity uncertainty in the probability of collision between space objects,” *AIAA/AAS Astrodynamics Specialist Conference 2014*, Vol. 143, San Diego, California, 2012, pp. 2159–2178.
- [37] Alfano, S., “Eliminating Assumptions Regarding Satellite Conjunction Analysis,” *The Journal of the Astronautical Sciences*, Vol. 59, 2014, pp. 676–705. <https://doi.org/10.1007/s40295-014-0002-4>.
- [38] Xu, X.-l., and Xiong, Y.-q., “A Research on the Collision Probability Calculation of Space Debris for Nonlinear Relative Motions†,” *Chinese Astronomy and Astrophysics*, Vol. 35, No. 3, 2011, pp. 304–317. <https://doi.org/10.1016/j.chinastron.2011.07.008>.
- [39] Wen, C., and Qiao, D., “Calculating collision probability for long-term satellite encounters through the reachable domain method,” *Astrodynamics*, Vol. 6, No. 2, 2022, pp. 141–159. <https://doi.org/10.1007/s42064-021-0119-8>.
- [40] Chan, K., “Short-term vs long-term spacecraft encounters,” *Collection of Technical Papers - AIAA/AAS Astrodynamics Specialist Conference*, Vol. 3, 2004, pp. 1732–1752.
- [41] Dolado, J. C., Legendre, P., Garmier, R., Revelin, B., and Pena, X., “Satellite collision probability computation for long term encounters,” *22nd AAS/AIAA Spaceflight Mechanics Meeting*, 2011.
- [42] Núñez Garzón, U. E., and Lightsey, E. G., “Relating Collision Probability and Separation Indicators in Spacecraft Formation Collision Risk Analysis,” *Journal of Guidance, Control, and Dynamics*, Vol. 45, No. 3, 2022, pp. 517–532. <https://doi.org/10.2514/1.G005744>.
- [43] Jones, B. A., and Doostan, A., “Satellite collision probability estimation using polynomial chaos expansions,” *Advances in Space Research*, Vol. 52, No. 11, 2013, pp. 1860–1875. <https://doi.org/10.1016/j.asr.2013.08.027>.
- [44] Adurthi, N., and Singla, P., “Conjugate unscented transformation-based approach for accurate conjunction analysis,” *Journal of Guidance, Control, and Dynamics*, Vol. 38, No. 9, 2015, pp. 1642–1658. <https://doi.org/10.2514/1.G001027>.

- [45] Vittaldev, V., and Russell, R. P., "Space object collision probability using multidirectional Gaussian mixture models," *Journal of Guidance, Control, and Dynamics*, Vol. 39, No. 9, 2016, pp. 2161–2167. <https://doi.org/10.2514/1.G001610>.
- [46] Armellin, R., Di Lizia, P., Bernelli-Zazzera, F., and Berz, M., "Asteroid close encounters characterization using differential algebra: The case of Apophis," *Celestial Mechanics and Dynamical Astronomy*, Vol. 107, No. 4, 2010, pp. 451–470. <https://doi.org/10.1007/s10569-010-9283-5>.
- [47] Wang, Z., and Grant, M. J., "Minimum-Fuel Low-Thrust Transfers for Spacecraft: A Convex Approach," *IEEE Transactions on Aerospace and Electronic Systems*, Vol. 54, No. 5, 2018, pp. 2274–2290. <https://doi.org/10.1109/TAES.2018.2812558>.
- [48] Mao, Y., and Acikmese, B., "SCvx-fast: A Superlinearly Convergent Algorithm for A Class of Non-Convex Optimal Control Problems," *ArXiv*, Vol. 2112, 2021. URL <http://arxiv.org/abs/2112.00108>.
- [49] He, Y., and Xu, M., "Bounded relative orbits in the zonal gravitational field for formation flying," *Journal of Guidance, Control, and Dynamics*, Vol. 41, No. 7, 2018, pp. 1629–1641. <https://doi.org/10.2514/1.G003107>.
- [50] Morselli, A., Armellin, R., Di Lizia, P., and Bernelli Zazzera, F., "A high order method for orbital conjunctions analysis: Sensitivity to initial uncertainties," *Advances in Space Research*, Vol. 53, No. 3, 2014, pp. 490–508. <https://doi.org/10.1016/j.asr.2013.11.038>.